

On the dynamics of the subtropical mode water from an ensemble view

Luolin Sun^{a,b,c}, Takaya Uchida^{b,d}, Thierry Penduff^b, William K. Dewar^{a,b}, Bruno Deremble^b,
Andrew C. Poje^e, Eric P. Chassignet^{a,c}, and Nicolas Wienders^c

^a *Department of Earth, Ocean and Atmospheric Science, Florida State University, Florida, USA*

^b *Université Grenoble Alpes, CNRS, INRAE, IRD, Grenoble INP, Institut des Géosciences de
l'Environnement, Grenoble, France*

^c *Center for Ocean-Atmospheric Prediction Studies, Florida State University, Florida, USA*

^d *Climate Dynamics Laboratory, Center for Earth Sciences, Moscow Institute of Physics and
Technology, Dolgoprudny, Russia*

^e *Department of Mathematics, College of Staten Island, The City University of New York, New
York, USA*

Corresponding author: Luolin Sun, ls24bk@fsu.edu

13 ABSTRACT: Subtropical mode water (STMW) in the North Atlantic has received particular
14 attention due to its formation through direct ocean-atmosphere interactions and its crucial role in
15 upper-ocean ventilation. Here, we diagnose the annual life cycle of STMW from a dynamical
16 perspective and investigate regional mechanisms governing its maintenance. We implement an
17 ensemble of 48 North Atlantic Ocean simulations at mesoscale-permitting resolution, forced by the
18 same atmospheric variability under slightly perturbed initial conditions. This ensemble approach,
19 together with the thickness-weighted averaging formalism, enables us to separate the spatiotempo-
20 rally dependent residual-mean flow from the residual-eddy fluctuations. We characterise STMW as
21 a pool of low potential vorticity (PV) in a buoyancy-coordinate framework within a defined control
22 volume. Our results reveal that the evolution of this low PV pool is primarily governed by the
23 residual-mean PV flux, associated with the residual-mean flow, and partially offset by residual-eddy
24 effects, as quantified by the residual-eddy PV flux. In an integrated and annually averaged sense,
25 the residual-mean PV flux extracts PV from the control volume, contributing to the formation of
26 STMW, whereas the residual-eddy PV flux mixes PV down the gradient, contributing to the erosion
27 of STMW. Diabatic effects become noticeable only when STMW layers are ventilated and exert
28 a comparatively weaker influence on STMW formation. The bolus eddy flux embedded within
29 the residual-mean PV flux becomes pronounced within the control volume of STMW during the
30 formation phase, contributing to PV homogenization by mixing newly formed low PV water with
31 the pre-existing counterpart.

1. Introduction

In the North Atlantic, the subtropical mode water (STMW) is a voluminous water mass characterised by nearly homogeneous properties in the upper ocean. It was initially referred to as the eighteen degree water (EDW) by Worthington (1958) since a large amount of water mass with temperature around 18°C was found in the Sargasso Sea. EDW plays a crucial role in regulating the upper ocean circulation by transporting atmospherically driven properties, such as temperature and carbon dioxide, from the surface to the interior (Hanawa and Talley 2001). It is directly ventilated at the surface in winter, then subducted from the mixed layer into the permanent thermocline in spring and summer. Given by the characteristic structure of the potential vorticity (PV) in the thermocline (Rhines and Young 1982; Luyten et al. 1983; Haynes and McIntyre 1987; Marshall et al. 2001), EDW can be characterised as a weakly stratified water mass with a local minimum PV. Its ventilation can be understood as a consequence of the atmosphere inducing low PV at the outcropping region which is then mixed with the surrounding higher PV by mesoscale eddies, resulting in a pool of homogeneous, low PV water (Peng et al. 2006).

Various studies have documented that the annual life cycle of EDW is associated with buoyancy loss and mixing processes in the Gulf Stream region where PV gradients are sharper and eddy activity is strong. Maze et al. (2009), Joyce (2013) and Forget et al. (2011) attributed EDW formation and erosion to the intense buoyancy-driven heat loss and gain at the surface south of the Gulf Stream. Billheimer and Talley (2016) found that vertical eddy mixing dominates the erosion of EDW and is more pronounced near Gulf Stream than in the southern subtropical gyre. The PV extraction due to such a buoyancy loss at surface has been hypothesised to be the source of EDW formation (Maze and Marshall 2011; Maze et al. 2013; Olsina et al. 2013), but was found to only marginally contribute to the total PV flux in Deremble and Dewar (2013). Despite these findings, the evolution of EDW and its relation associated with the Gulf Stream and the subtropical recirculation have not been fully addressed, which will be one of the main focuses of this study.

The role of eddies in EDW formation was initially discussed within a quasi-geostrophic framework by Dewar (1986). By assuming a downgradient eddy PV flux, the maintenance of the low-PV pool was demonstrated by a balance between eddy PV fluxes and buoyant PV forcing. Maze et al. (2013) was the first to use a realistic ocean model to quantify eddy effects, comparing surface PV fluxes computed from an eddy-permitting (1/12°) model with those derived from the non-eddy-

62 resolving OCCA dataset (Forget 2010), and suggested that eddy contributions were secondary. In
63 contrast, Deremble and Dewar (2013), using an eddy-resolving ocean model, found that eddies
64 contributed approximately one-quarter of the total PV budget and hypothesized that the mainte-
65 nance of EDW results from a lateral balance between the mean flow and eddies, consistent with
66 earlier QG results Dewar (1986). In their study, eddies and the mean flow were separated using
67 a thickness-weighted time-averaging operator. Building on these insights, we are motivated to
68 consider a time-dependent mean-eddy separation to explicitly study the temporal effects of the
69 mean flow and eddies on the annual cycle of STMW. In addition, we will investigate the role of
70 eddies in subducting surface-formed EDW into the main thermocline.

71 In this study, we quantify the North Atlantic Subtropical Mode Water by identifying it as a low
72 potential vorticity pool, and hence refer to it as STMW rather than Eighteen Degree Water (EDW),
73 as our definition is based on PV structure rather than temperature homogeneity. To examine the
74 respective roles of the mean flow and eddies, we employ an ensemble of eddy-permitting North
75 Atlantic simulations. The mean flow is defined as the spatiotemporally varying ensemble-mean
76 variable, enabling us to separate eddy fields without prescribing assumptions on their temporal or
77 spatial scales.

78 The ensemble-averaging approach adopted in this study naturally leads to the use of the thickness-
79 weighted averaging (TWA) framework (Young 2012), in which dynamical variables are both
80 thickness-weighted and ensemble-averaged within buoyancy layers. This TWA framework yields
81 a PV conservation analogous to that of the Ertel’s potential vorticity, traditionally used to study
82 the PV budget associated with EDW formation and evolution (Marshall et al. 2001; Czaja and
83 Hausmann 2009; Maze and Marshall 2011; Olsina et al. 2013; Deremble and Dewar 2013). Water-
84 mass formation (Walin 1982), the primary factor of STMW formation (Joyce et al. 2013; Maze
85 and Marshall 2011), is implicitly embedded in the TWA formalism, and is naturally connected to
86 the TWA’s PV conservation. Specifically, the thickening of water masses due to surface buoyancy
87 variations is reflected as an increase in layer thickness, which, given thickness-weighted PV
88 conservation within the layer, leads to a decrease in the TWA’s PV. The framework implemented
89 in this study captures the key characteristics of the STMW annual life cycle, linking the seasonal
90 thickening and thinning of layers directly to the evolution of PV.

91 The article is structured as follows. In Section 2, we introduce the ensemble simulations used
 92 in this study and briefly review the TWA formalism. In Section 3, we characterize the simulated
 93 STMW and describe its annual life cycle. Later in the section, we define a control volume for a
 94 low PV pool within a STMW layer. This is then followed by a diagnosis of the evolution of the
 95 PV budget within this control volume in Section 4, with the results interpreted in terms of the
 96 annual characteristics of STMW formation and erosion. In Section 5, we investigate the regional
 97 mechanisms governing STMW maintenance within the subtropical gyre. In Section 6, we discuss
 98 the role of the eddy-induced bolus velocity on the lateral PV mixing during the formation phase
 99 of STMW. We discuss technical challenges related to closing the PV budget in Section 7, and
 100 summarise the main findings of the study in Section 8.

101 **2. Methodology**

102 We begin this section by describing the ensemble simulations used in the study and introducing
 103 the ensemble-based separation of mean and eddy components. We then revisit the thickness-
 104 weighted averaging framework introduced by Young (2012) and derive the corresponding potential
 105 vorticity equation. Mathematical notations are summarized in Table 1.

106 *a. Ensemble simulations*

107 We employ an ensemble of North Atlantic simulations (NA12), which covers the latitudes of
 108 20°S to 55°N as described in Jamet et al. (2019, 2020) and Uchida et al. (2025), using the
 109 Massachusetts Institute of Technology general circulation model (MITgcm; Marshall et al. 1997).
 110 These simulations are mesoscale-permitting at 1/12° and partially coupled to the atmosphere via
 111 the Cheap Atmospheric Mixed Layer model (Deremble et al. 2013). Forty-eight ensemble members
 112 are initialized with distinct but physically consistent oceanic states, exposed to the same prescribed
 113 atmospheric variability beginning on January 1st, 1963 and then simulated onwards for five years.
 114 Instantaneous snapshots of the model state are saved every five days during the last year, 1967, and
 115 are the model outputs used in this study.

116 We follow the prescription described in Uchida et al. (2022, 2023) to interpolate the variable out-
 117 puts from geopotential coordinates (t, x, y, z) into buoyancy coordinates represented by $(\tilde{t}, \tilde{x}, \tilde{y}, \tilde{b})$.
 118 Here, \tilde{b} is the thermodynamically and dynamically consistent buoyancy; it is defined via in-situ

density anomaly (see also Stanley and Marshall 2022), which is close to being a neutral surface and has a monotonic relation with depth z as discussed in Uchida et al. (2022). \tilde{x} and \tilde{y} are the lateral coordinates on the \tilde{b} -surfaces. We assign the same \tilde{b} -coordinate system to all ensemble members. Consequently, the corresponding depths are considered to be a function of \tilde{b} . For each ensemble member, indexed by n , the depth z is transformed from geopotential coordinates to \tilde{b} -coordinates as

$$z_n = \zeta_n(\tilde{t}, \tilde{x}, \tilde{y}, \tilde{b}), \quad n = 1, \dots, N, \quad (1)$$

and the thickness of a buoyancy layer centered at \tilde{b} is defined as

$$\sigma_n(\tilde{t}, \tilde{x}, \tilde{y}, \tilde{b}) \stackrel{\text{def}}{=} \frac{\partial \zeta_n}{\partial \tilde{b}}, \quad n = 1, \dots, N, \quad (2)$$

where $N = 48$ is the total number of ensemble members.

The ensemble-based Reynolds' decomposition is well suited for the present study of the evolution of STMW, as it enables a separation between mean variables and eddy fields at any location and time without making implicit assumptions about their spatial or temporal scales. A full velocity field \mathbf{u}_n is decomposed into an ensemble-mean field

$$\langle \mathbf{u} \rangle \stackrel{\text{def}}{=} \frac{1}{N} \sum_{n=1}^N \mathbf{u}_n, \quad (3)$$

where $\langle \cdot \rangle$ denotes the ensemble-averaging operator, and an ensemble-eddy field

$$\mathbf{u}'_n \stackrel{\text{def}}{=} \mathbf{u}_n - \langle \mathbf{u} \rangle. \quad (4)$$

$\langle \mathbf{u} \rangle$ can be considered as the common oceanic response among members to the same prescribed atmospheric variability, and \mathbf{u}'_n as the ocean-generated intrinsic eddies (Penduff et al. 2011; Leroux et al. 2018; Constantinou and Hogg 2021). Similarly, the ensemble-mean depth and layer thickness

135 are given by

$$\langle \zeta \rangle \stackrel{\text{def}}{=} \frac{1}{N} \sum_{n=1}^N \zeta_n, \quad (5a)$$

$$\langle \sigma \rangle \stackrel{\text{def}}{=} \frac{1}{N} \sum_{n=1}^N \sigma_n, \quad (5b)$$

136 and their eddy fluctuations around their ensemble-mean fields are given by

$$\zeta'_n \stackrel{\text{def}}{=} \zeta_n - \langle \zeta \rangle, \quad (6a)$$

$$\sigma'_n \stackrel{\text{def}}{=} \sigma_n - \langle \sigma \rangle. \quad (6b)$$

137 $\langle \zeta \rangle$ and $\langle \sigma \rangle$ characterise the common features of the stratifications among the ensemble members,
 138 and ζ'_n and σ'_n are displacements around them. These variables play a key role in the TWA
 139 framework as well as in the analysis of STMW dynamics. Before we delve into the details of TWA
 140 formalism, we remind readers that all calculations of the variables and their analyses throughout
 141 this study are carried out in \tilde{b} -coordinate system.

142 *b. Governing equations*

143 1) MOMENTUM EQUATIONS

144 In TWA, the primitive equations are reformulated as the following lateral residual-mean momen-
 145 tum equations and the ensemble-mean thickness equation:

$$\hat{u}_{\tilde{t}} + \hat{u}\hat{u}_{\tilde{x}} + \hat{v}\hat{u}_{\tilde{y}} + \hat{\omega}\hat{u}_{\tilde{b}} - f\hat{v} + \langle m \rangle_{\tilde{x}} + \nabla \cdot \mathbf{E}^u = \hat{\mathcal{X}}, \quad (7a)$$

$$\hat{v}_{\tilde{t}} + \hat{u}\hat{v}_{\tilde{x}} + \hat{v}\hat{v}_{\tilde{y}} + \hat{\omega}\hat{v}_{\tilde{b}} + f\hat{u} + \langle m \rangle_{\tilde{y}} + \nabla \cdot \mathbf{E}^v = \hat{\mathcal{Y}}, \quad (7b)$$

$$\langle \sigma \rangle_{\tilde{t}} + \langle \sigma \rangle \nabla \cdot \hat{\mathbf{u}} = 0, \quad (7c)$$

146 where the subscripts denote the partial differentiations in \tilde{b} -coordinates and $\widehat{(\cdot)}$ denotes a TWA
 147 operator. Note that (7c) appears slightly differently in Young (2012) where we have used the vector

148 notation (12). \hat{u} , \hat{v} and $\hat{\varpi}$ are residual-mean velocities of the form

$$\hat{\theta} \stackrel{\text{def}}{=} \frac{\langle \sigma \theta \rangle}{\langle \sigma \rangle}, \quad \theta \in \{u, v, \varpi\}, \quad (8)$$

149 and $\hat{\mathbf{u}} \stackrel{\text{def}}{=} (\hat{u}, \hat{v}, \hat{\varpi})$ is referred to as the TWA velocity. The thickness equation (7c) shows that the
 150 divergence of the TWA velocity governs the per unit rate of change in thickness

$$-\langle \sigma \rangle^{-1} \langle \sigma \rangle_{\bar{t}} = \nabla \cdot \hat{\mathbf{u}} \neq 0, \quad (9)$$

151 and is generally non-zero. The divergence-free velocity field in TWA is instead represented by the
 152 residual velocity $\mathbf{u}^\# \stackrel{\text{def}}{=} \hat{u} \langle \mathbf{e} \rangle_1 + \hat{v} \langle \mathbf{e} \rangle_2 + \langle \sigma \rangle^{-1} (\langle \zeta_{\bar{t}} \rangle + \hat{\varpi} \langle \zeta \rangle_{\bar{b}}) \langle \mathbf{e} \rangle_3$ as defined in Young (2012), which
 153 aligns with $\hat{\mathbf{u}}$ if the flow is steady and adiabatic (Aoki 2014). In this study, we only use $\hat{\mathbf{u}}$ in the
 154 formalism of TWA velocity.

155 The eddy forcing is given by the divergences of the three-dimensional Eliassen-Palm (E-P) flux
 156 tensors,

$$\mathbf{E}^u \stackrel{\text{def}}{=} \left(\overline{u''u''} + \frac{\langle \zeta'^2 \rangle}{2\langle \sigma \rangle} \right) \langle \mathbf{e} \rangle_1 + \overline{v''u''} \langle \mathbf{e} \rangle_2 + \left(\overline{\varpi''u''} + \frac{\langle \zeta' m'_{\bar{x}} \rangle}{\langle \sigma \rangle} \right) \langle \mathbf{e} \rangle_3, \quad (10a)$$

$$\mathbf{E}^v \stackrel{\text{def}}{=} \overline{u''v''} \langle \mathbf{e} \rangle_1 + \left(\overline{v''v''} + \frac{\langle \zeta'^2 \rangle}{2\langle \sigma \rangle} \right) \langle \mathbf{e} \rangle_2 + \left(\overline{\varpi''v''} + \frac{\langle \zeta' m'_{\bar{y}} \rangle}{\langle \sigma \rangle} \right) \langle \mathbf{e} \rangle_3. \quad (10b)$$

157 $\mathbf{u}_n'' \stackrel{\text{def}}{=} (u_n'', v_n'', \varpi_n'')$ is the residual-eddy velocity for each ensemble member with the components

$$(u_n'', v_n'', \varpi_n'') \stackrel{\text{def}}{=} (u_n, v_n, \varpi_n) - (\hat{u}, \hat{v}, \hat{\varpi}), \quad (11)$$

158 and modifies the corresponding thickness fluctuation σ_n' . A schematic of the coordinate transfor-
 159 mation and the decomposition between the residual-mean and the residual-eddy velocities is shown
 160 in Figure 1.

161 The divergence operator is in the form

$$\nabla \cdot \left(E^1 \langle \mathbf{e} \rangle_1 + E^2 \langle \mathbf{e} \rangle_2 + E^3 \langle \mathbf{e} \rangle_3 \right) \stackrel{\text{def}}{=} \langle \sigma \rangle^{-1} (\langle \sigma \rangle E^1)_{\bar{x}} + \langle \sigma \rangle^{-1} (\langle \sigma \rangle E^2)_{\bar{y}} + \langle \sigma \rangle^{-1} (\langle \sigma \rangle E^3)_{\bar{b}}, \quad (12)$$

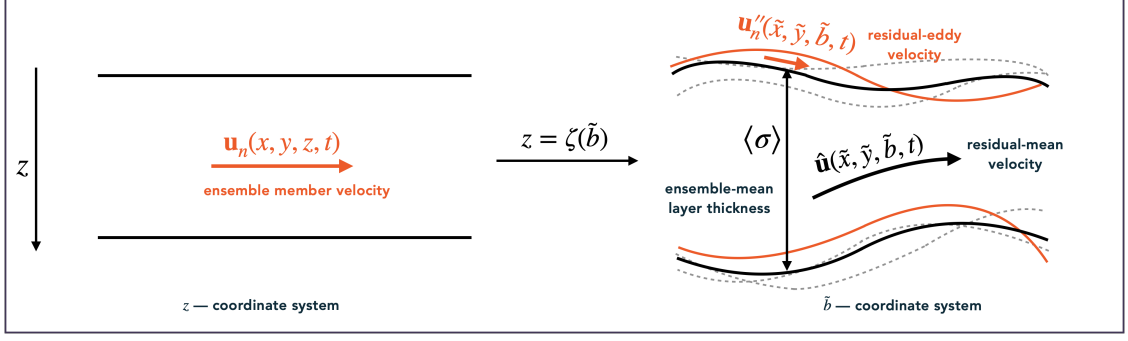


FIG. 1. Conceptual schematic illustration of the TWA formalism. The velocity field \mathbf{u}_n of an ensemble member in geopotential coordinates (left panel) is transformed into buoyancy coordinates, where it is separated into a residual-mean velocity $\hat{\mathbf{u}}$ and a residual-eddy velocity \mathbf{u}_n'' (right panel). Quantities and curves shown in orange are specific to the individual ensemble member, while those in black represent ensemble-mean properties shared across members. The vertical structure of the buoyancy coordinates (black curves) is determined by the ensemble-mean layer thickness $\langle \sigma \rangle$. Dashed lines denote layers from other ensemble members.

where $\langle \mathbf{e} \rangle_1 = \mathbf{i} + \langle \zeta \rangle_{\tilde{x}} \mathbf{k}$, $\langle \mathbf{e} \rangle_2 = \mathbf{j} + \langle \zeta \rangle_{\tilde{y}} \mathbf{k}$ and $\langle \mathbf{e} \rangle_3 = \langle \sigma \rangle \mathbf{k}$ are the vector basis of the \tilde{b} -coordinate system.

The Montgomery potential is related to the dynamically active part of hydrostatic pressure, ϕ , via

$$m(\tilde{t}, \tilde{x}, \tilde{y}, \tilde{b}) \stackrel{\text{def}}{=} \phi(t, x, y, \zeta) - \tilde{b} \zeta(\tilde{t}, \tilde{x}, \tilde{y}, \tilde{b}); \quad (13)$$

and $\hat{\mathcal{X}}$ and $\hat{\mathcal{Y}}$ are the adiabatic terms.

2) POTENTIAL VORTICITY EQUATION

Subtracting the cross derivatives of equations (7a) and (7b) gives the definition of the PV in TWA formalism

$$\Pi^\# \stackrel{\text{def}}{=} \frac{f + \hat{v}_{\tilde{x}} - \hat{u}_{\tilde{y}}}{\langle \sigma \rangle}, \quad (14)$$

and leads to a conservation equation for PV of $\hat{\mathbf{u}}$,

$$\langle \sigma \rangle^{-1} (\langle \sigma \rangle \Pi^\#)_{\tilde{t}} + \nabla \cdot \mathbf{J}^\# + \nabla \cdot \mathbf{F}^\# + \nabla \cdot \mathbf{G}^\# = 0. \quad (15)$$

Equation (15) is analogous to the conservation form of the Ertel's PV discussed in Haynes and McIntyre (1987); Marshall et al. (2001). The impermeability theorem holds here so $\Pi^\#$ of the buoyancy layer can only be modified at the ocean boundaries. We remind readers that $\Pi^\#$ is not a mean quantity of PV but rather the PV associated with the residual-mean flow $\hat{\mathbf{u}}$ (viz. $\Pi^\# \neq \widehat{\Pi}$; Young 2012), as the TWA operator does not commute with cross-product (Maddison and Marshall 2013). Throughout the following discussion, we refer to $\Pi^\#$ simply as 'PV' for brevity.

The residual-mean PV flux

$$\mathbf{J}^\# \stackrel{\text{def}}{=} \hat{u}\Pi^\#\langle\mathbf{e}\rangle_1 + \hat{v}\Pi^\#\langle\mathbf{e}\rangle_2 + \hat{w}\Pi^\#\langle\mathbf{e}\rangle_3, \quad (16)$$

quantifies the advection of $\Pi^\#$ by the TWA velocity $\hat{\mathbf{u}}$. It consists both the large-scale advection by the ensemble-mean velocity $\langle\mathbf{u}\rangle$ and the lateral eddy-induced advection by the bolus velocity

$$\mathbf{u}^* \stackrel{\text{def}}{=} \frac{\langle\sigma'\mathbf{u}'_h\rangle}{\langle\sigma\rangle} = \hat{\mathbf{u}} - \langle\mathbf{u}\rangle, \quad (17)$$

where $\mathbf{u}'_h \stackrel{\text{def}}{=} u'\langle\mathbf{e}\rangle_1 + v'\langle\mathbf{e}\rangle_2$ is along \tilde{b} -surfaces. In TWA, \mathbf{u}^* is designed to be embedded in $\hat{\mathbf{u}}_h$ because variations of buoyancy-driven layers should naturally be incorporated into mean (TWA) variables.

The residual-eddy PV flux

$$\mathbf{F}^\# \stackrel{\text{def}}{=} \left(\langle\sigma\rangle^{-1}\nabla\cdot\mathbf{E}^v\right)\langle\mathbf{e}\rangle_1 - \left(\langle\sigma\rangle^{-1}\nabla\cdot\mathbf{E}^u\right)\langle\mathbf{e}\rangle_2, \quad (18)$$

quantifies the effects of the eddy forcing appeared in the momentum equations (7) on the PV transport. The diabatic PV flux is given by

$$\mathbf{G}^\# \stackrel{\text{def}}{=} \langle\sigma\rangle^{-1} \left(-\hat{\mathcal{Y}} + \hat{v}_{\tilde{b}}\hat{w}\right)\langle\mathbf{e}\rangle_1 + \langle\sigma\rangle^{-1} \left(\hat{\mathcal{X}} - \hat{u}_{\tilde{b}}\hat{w}\right)\langle\mathbf{e}\rangle_2 - \hat{w}\Pi^\#\langle\mathbf{e}\rangle_3. \quad (19)$$

By applying the chain rule to $(\langle\sigma\rangle\Pi^\#)_{\tilde{t}}$ and using the thickness equation in the form (9), we rewrite the PV equation (15) in an equivalent form

$$\Pi^\#_{\tilde{t}} - \Pi^\#\nabla\cdot\hat{\mathbf{u}} + \nabla\cdot\mathbf{J}^\# + \nabla\cdot\mathbf{F}^\# + \nabla\cdot\mathbf{G}^\# = 0. \quad (20)$$

194 Apart from the flux divergences, the rate of PV is also associated with the PV-weighted divergence
 195 of the TWA velocity. We use equation (20) to study the PV budget. This is because in the STMW
 196 analysis the low PV pool is conventionally determined by the potential vorticity, that is, $\Pi^\#$ in our
 197 case, rather than the absolute vorticity $\langle \sigma \rangle \Pi^\#$ in the tendency term in equation (15).

TABLE 1. Summary of key notations and variables used in the study

Mathematical symbol	Description
\tilde{b}	Thermodynamically and dynamically consistent buoyancy
z	Depth in geopotential coordinates
ζ	Depth in \tilde{b} -coordinates
$\sigma \stackrel{\text{def}}{=} \zeta_{\tilde{b}}$	Thickness of buoyancy layers
$\langle \cdot \rangle$	Ensemble-averaging operator
$\overline{(\cdot)}$	Thickness-weighted ensemble-averaging (TWA) operator
$\overline{(\cdot)}$	Time-averaging operator
$\langle \sigma \rangle$	Ensemble-mean thickness
\hat{u}	Residual-mean velocity component
$\mathbf{u} \stackrel{\text{def}}{=} (u, v, \varpi)$	Three-dimensional velocity field in \tilde{b} -coordinates
$\langle \mathbf{u} \rangle \stackrel{\text{def}}{=} (\langle u \rangle, \langle v \rangle, \langle \varpi \rangle)$	Three-dimensional ensemble-mean velocity
$\mathbf{u}' \stackrel{\text{def}}{=} \mathbf{u} - \langle \mathbf{u} \rangle$	Three-dimensional ensemble-eddy velocity
$\hat{\mathbf{u}} \stackrel{\text{def}}{=} (\hat{u}, \hat{v}, \hat{\varpi})$	Three-dimensional TWA velocity
$\mathbf{u}'' \stackrel{\text{def}}{=} \mathbf{u} - \hat{\mathbf{u}}$	Three-dimensional residual-eddy velocity
$\hat{\mathbf{u}}_h \stackrel{\text{def}}{=} (\hat{u}, \hat{v})$	Lateral TWA velocity on \tilde{b} -surfaces
\mathbf{u}^*	Two-dimensional bolus-eddy velocity
$\mathbf{E}^u, \mathbf{E}^v$	Eliassen-Palm flux tensors
$(\cdot)^\#$	Non-TWA variables consisting the residual field
$\Pi^\#$	Potential vorticity on a buoyancy layer with ensemble-mean thickness $\langle \sigma \rangle$
$\mathbf{J}^\#$	Residual-mean PV flux
$\mathbf{F}^\#$	Residual-eddy PV flux
$\mathbf{G}^\#$	Diabatic PV flux
$\mathbf{u}^* \Pi^\#$	Bolus-eddy PV flux
$\langle \mathbf{u} \rangle \Pi^\#$	Ensemble-mean PV flux
Ω	Control volume of PV pool in the core STMW layer

198 3. Characterising STMW in TWA

199 In this section, we characterise STMW layers in the TWA framework and outline their annual
 200 cycle. We then determine a control volume of a low PV pool in the core layer of STMW. The
 201 dynamics of PV evolution within this control volume will be the focus of the study.

202 *a. Model evaluation*

203 We evaluate the NA12 simulation over year 1967 by comparing the monthly-mean temperature
204 profiles averaged over all ensemble members with the observation-based Met Office EN4 dataset
205 of $1^\circ \times 1^\circ$ resolution (Good et al. 2013; Cheng et al. 2014). Figure 2 compares NA12 and
206 EN4 in terms of sea surface temperatures (SST) in February and vertical sections of February
207 and September potential temperatures zonally averaged between 75°W and 50°W . Overall, the
208 ensemble-mean temperature $\langle T \rangle$ from NA12 exhibits a warm bias of up to 3°C and a more
209 pronounced stratification compared to observations. The temperature of the simulated STMW
210 varies between 20°C and 22°C , and accordingly, the winter outcrop is found about 2° south of its
211 observed latitude (see panels 2a and 2d).

212 Despite these differences, the vertical and latitudinal structures of stratification are similar be-
213 tween EN4 and NA12. In both datasets the isopycnals where the STMW resides outcrop between
214 30°N and 40°N in winter (panels 2b and 2e), and the water masses are isolated in summer (pan-
215 els 2c and 2f). Hence, we argue that despite its warm bias, the model dynamics that control the
216 life cycle of the STMW are relevant for the real-world setting. These ensemble simulations were
217 also shown to be highly correlated with the RAPID-MOCHA observations of AMOC (Jamet et al.
218 2019), further supporting the dynamical relevance of the simulation in this region.

222 *b. Simulated STMW layers*

223 Since STMW is formed when the mixed layer deepens in winter, determining the mixed layer
224 depth (MLD) is crucial for understanding the formation mechanism. We determine the MLD for
225 the ensemble as follows. We first estimate the MLD for each ensemble member as a time-varying
226 surface in \tilde{b} -coordinates, where the potential density becomes 0.03 kg m^{-3} larger than that at 10 m
227 depth (de Boyer Montégut et al. 2004). Then, to mitigate the influence of local extrema in individual
228 MLD estimates across the ensemble, we define the ensemble MLD as the third quantile of the 48
229 member estimates¹. The mixed layer presents a subtlety for the TWA analysis that the vertical
230 displacement can not be perfectly resolved by the buoyancy within the mixed layer. That is, as the
231 mixed layer intrudes the region of the STMW, the numerical accuracy of the STMW estimation

¹As the MLDs in some members are deeper than others, we have opted for the third quantile instead of the ensemble-mean to ensure that the layers beneath the mixed layer remain substantial within the ensemble. This approach is conceptually similar to using the ensemble mean under a Gaussian distribution, where the second quantile is identical to with the mean.

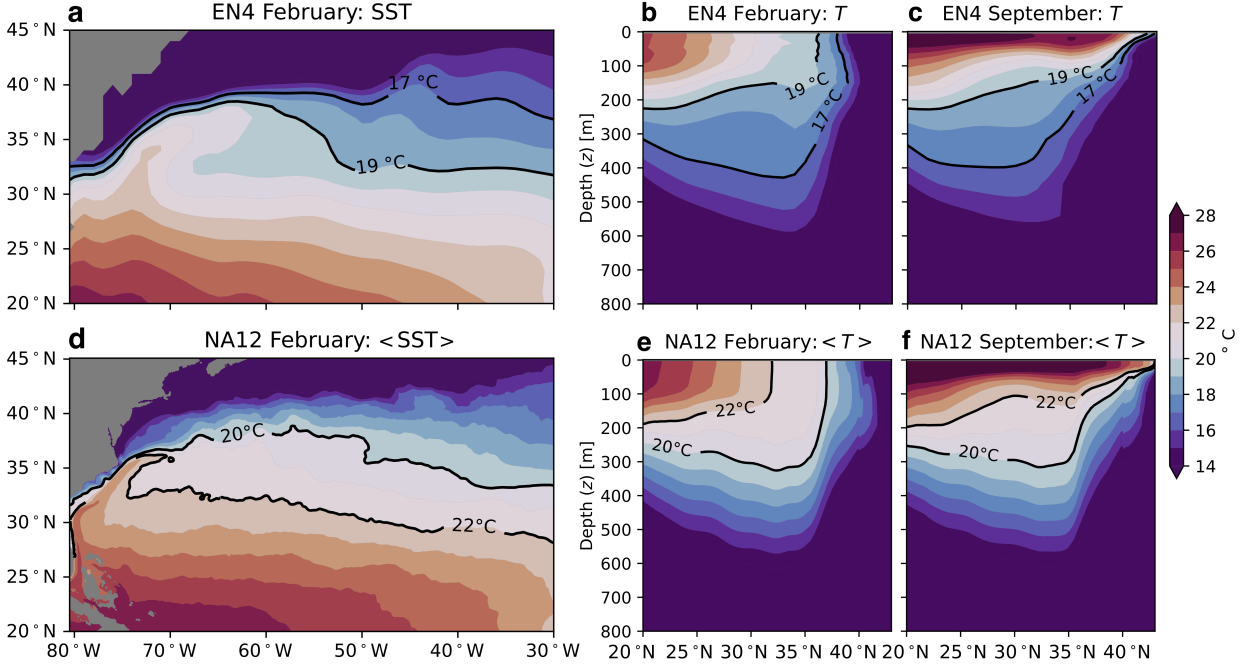


FIG. 2. Sea surface temperature in February 1967 for (a) EN4 and (d) N12. Monthly temperatures zonally averaged between 75°W and 50°W for EN4 (b,c) and NA12 (e,f). Black contours show the temperature range of the STMW.

will become less promising. In this study, we choose to retain the STMW within the mixed layer, and the rationale for this choice will be explained later in the section.

We identify the simulated STMW by its associated local PV minimum on \tilde{b} -surfaces. Figure 3 shows the zonally averaged structure of PV on \tilde{b} -surfaces for each month. The two pink lines identify the top and the bottom surfaces of the STMW, and are in correspondence to the isolines of the temperatures in Figure 2. The PV is minimum along the surface $\tilde{b} = -0.25 \text{ m s}^{-2}$ which identifies the center of the core layer, shown as red lines in Figure 3. The buoyancy \tilde{b} of the layers within which the STMW sits varies between -0.253 m s^{-2} and -0.247 m s^{-2} . Between February and April, STMW layers slant greatly starting at 30°N, intrude into the deepening mixed layer (its depth is coloured in grey) and get directly ventilated at the ocean surface near 35°N. They are then subducted towards the ocean interior from May when the mixed layer becomes shallow. As a consequence of this process, the total thickness of the STMW peaks in June and slowly decreases afterwards, in accordance with the formation and erosion of the STMW. Overall, these results

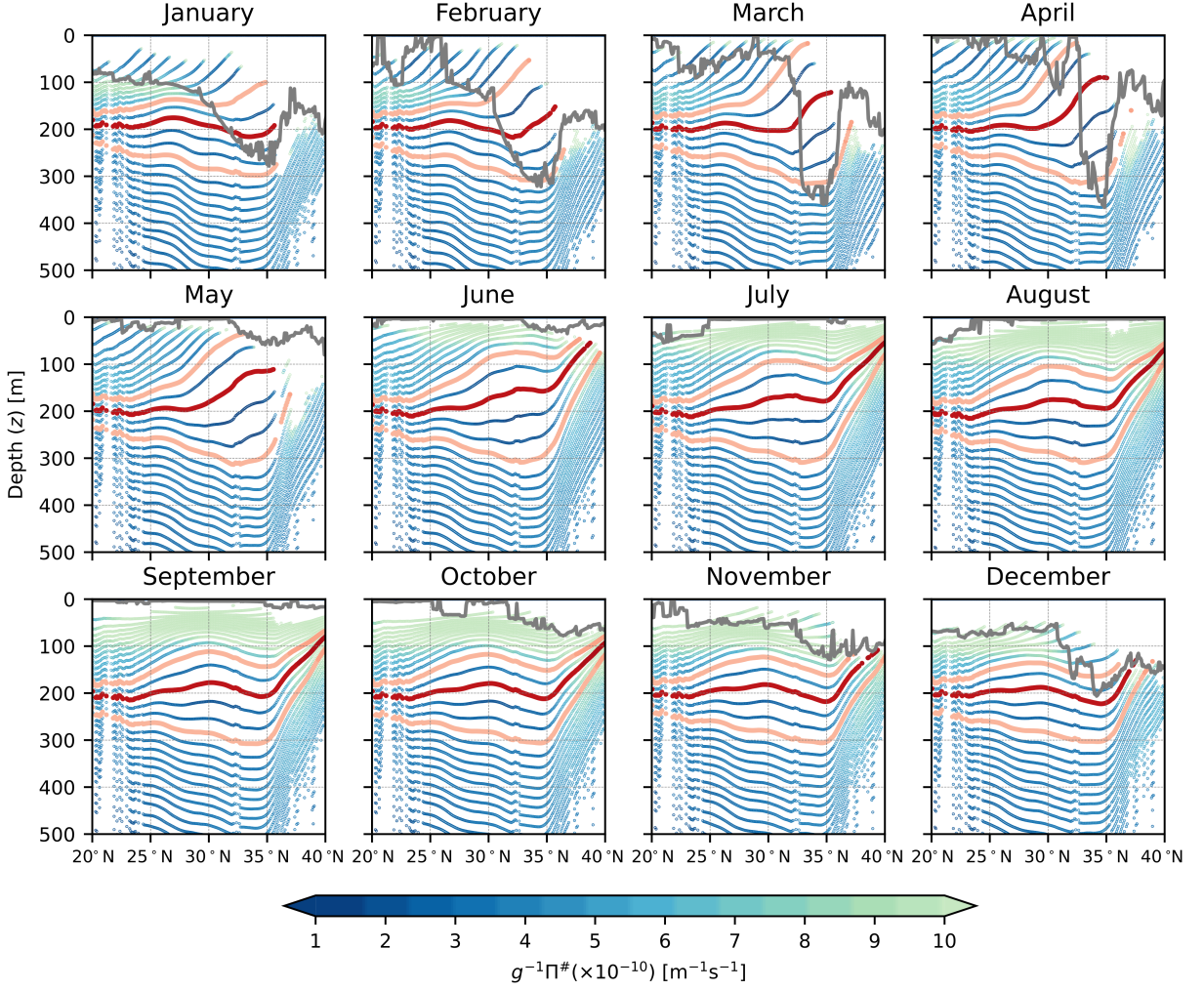


FIG. 3. $\Pi^\#$ is divided by g to adopt the conventional unit $[\text{m}^{-1}\text{s}^{-1}]$ for PV. Blue-green lines show the monthly-averaged PV structure along \tilde{b} -surfaces, zonally averaged between 75°W and 50°W . This is the same region chosen for averaging the potential temperatures in Figure 2. Pink lines indicate the centers of the top and bottom layers of the STMW, and the red lines the centers of the core layer $\tilde{b} = -0.25 \text{ m s}^{-2}$. The bottom of the zonal mean of the third quantile of MLD is plotted in gray. We remind the reader that the MLD is estimated locally in space-time and then zonally and monthly averaged when plotting. The tips of the lines near the surface show where the layers reaches outcrop region.

demonstrate that the annual life cycle of the STMW is adequately characterised by the PV defined in the thickness-weighted ensemble-averaging framework.

254 *c. Control volume of low PV pool*

255 To study the dynamics of the STMW, we focus our study on the core layer. Because it is rarely
 256 contaminated by outcropping, where PV becomes ill-defined in the layers above, the analysis can
 257 be done for all months in the year. It is also the most representative layer among STMW layers
 258 since its thickness varies the most in time. We determine a control volume of a low PV pool in this
 259 layer as follows.

260 The annual-mean ensemble-mean thickness $\overline{\langle \sigma \rangle}$ of the core layer and the annual-mean PV,
 261 $\overline{g^{-1}\Pi^{\#}}$, are shown on the center surface in Figure 4. $\overline{(\cdot)}$ denotes the temporal averaging and $\Pi^{\#}$ is
 262 divided by g to adopt the conventional unit [$\text{m}^{-1}\text{s}^{-1}$] for PV. We restrict our analysis over a region
 263 in the core layer that does not outcrop over the year and subsequently exclude the area shaded
 264 in light gray in panel (b) from the analysis. We determine the PV threshold of the STMW as
 265 $g^{-1}\Pi^{\#} \leq 3 \times 10^{-10} \text{ m}^{-1} \text{ s}^{-1}$. This threshold is larger than those used in some other studies (Hanawa
 266 and Talley 2001; Kwon and Riser 2004; Forget et al. 2011; Maze et al. 2013; Billheimer and Talley
 267 2013; Li et al. 2022) because PV is more stratified in our study. The contour (plotted in black)
 268 determined with this threshold for the annual-mean $\overline{g^{-1}\Pi^{\#}}$ serves as the lateral boundary C of
 269 the control volume. Together with the time-varying thickness $\langle \sigma \rangle$ shown in panel (a), the control
 270 volume Ω encloses the low PV water in the core layer.

280 Figure 5 illustrates the monthly evolution of STMW ($\Pi^{\#} \leq 3 \times 10^{-10} \text{ m}^{-1} \text{ s}^{-1}$, colored in dark blue)
 281 in the core layer on $\tilde{b} = -0.25 \text{ m s}^{-2}$. A portion of STMW persists year-round along the coast
 282 between 25°N and 35°N , 80°W and 70°W , and in the southern Sargasso Sea between 25°N and
 283 30°N , 70°W and 60°W . In January, low PV water induced by surface buoyancy loss (Maze and
 284 Marshall 2011; Maze et al. 2013) begins to emerge northeast of the control volume and occupies the
 285 ‘formation zone’ by February, as outlined by the green box. This newly formed low PV water then
 286 migrates southward and connects with the pre-existing low PV water. The PV minimum during
 287 this phase is located near 35°N , 60°W , consistent with the region where Warren (1972) identified
 288 the winter formation of STMW. Between March and May, the STMW expands as more low PV
 289 water is injected into the system, reaching its maximum extent in June. From July to August, PV
 290 within the STMW gradually increases as it mixes with surrounding high PV waters. Beginning
 291 in September, STMW undergoes noticeable erosion, starting in the ‘formation zone’ as the layer

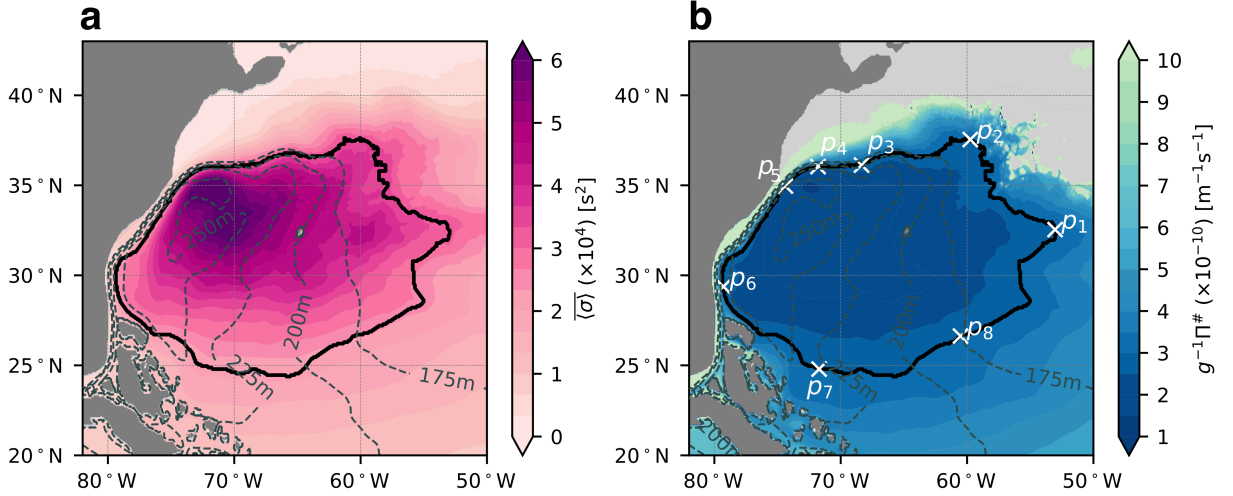


FIG. 4. Annual mean of (a) layer thickness $\overline{\langle \sigma \rangle}$ and (b) PV $\overline{g^{-1}\Pi^\#}$ on surface $\tilde{b} = -0.25 \text{ m s}^{-2}$ centered in the core STMW layer. Black contours are the boundaries of STMW with the threshold $g^{-1}\Pi^\# = 3 \times 10^{-10} \text{ m}^{-1} \text{ s}^{-1}$. Grey dashed lines label the depth of this \tilde{b} -surface. p -indices in white are critical locations along the contour, and are labelled by numbers in a counter-clockwise direction following the integration along the contour. Segment from p_7 to p_5 traces the Florida Current along the coastline and p_5 is near Cape Hatteras. Segment from p_5 to p_2 is on the southern flank of the Gulf stream. The separation point where the Gulf Stream detaches from the coast and migrates eastward is between p_5 and p_4 . Low PV water formed in early winter enters the control volume from the north through segment between p_2 and p_1 . Segment p_1 to p_7 approximately follows the recirculation of the subtropical gyre.

subducts, and continues to shrink, reaching its minimum extent by December—thus setting the stage for renewal in the following year.

An important assumption for PV conservation within a control volume is that the volume must be enclosed by a geostrophic contour, such as a PV streamline, together with two neutral surfaces (Luyten et al. 1983; Stanley et al. 2020; Stanley and Marshall 2022). However, determining a time-evolving geostrophic contour is technically challenging, particularly when \tilde{b} -surfaces outcrop at the surface. We thus lead to adopt a fixed lateral boundary in time, defined by a time-mean PV threshold. Consequently, the boundary does not evolve dynamically with the actual PV field within the threshold, and strict PV conservation within our control volume cannot be expected. To ensure that our analysis remains robust despite this limitation, we repeated the calculations using alternative PV thresholds, i.e., $g^{-1}\Pi^\# \leq \{1.8, 2.0, 2.5\} \times 10^{-10} \text{ m}^{-1} \text{ s}^{-1}$. In all cases, we obtained

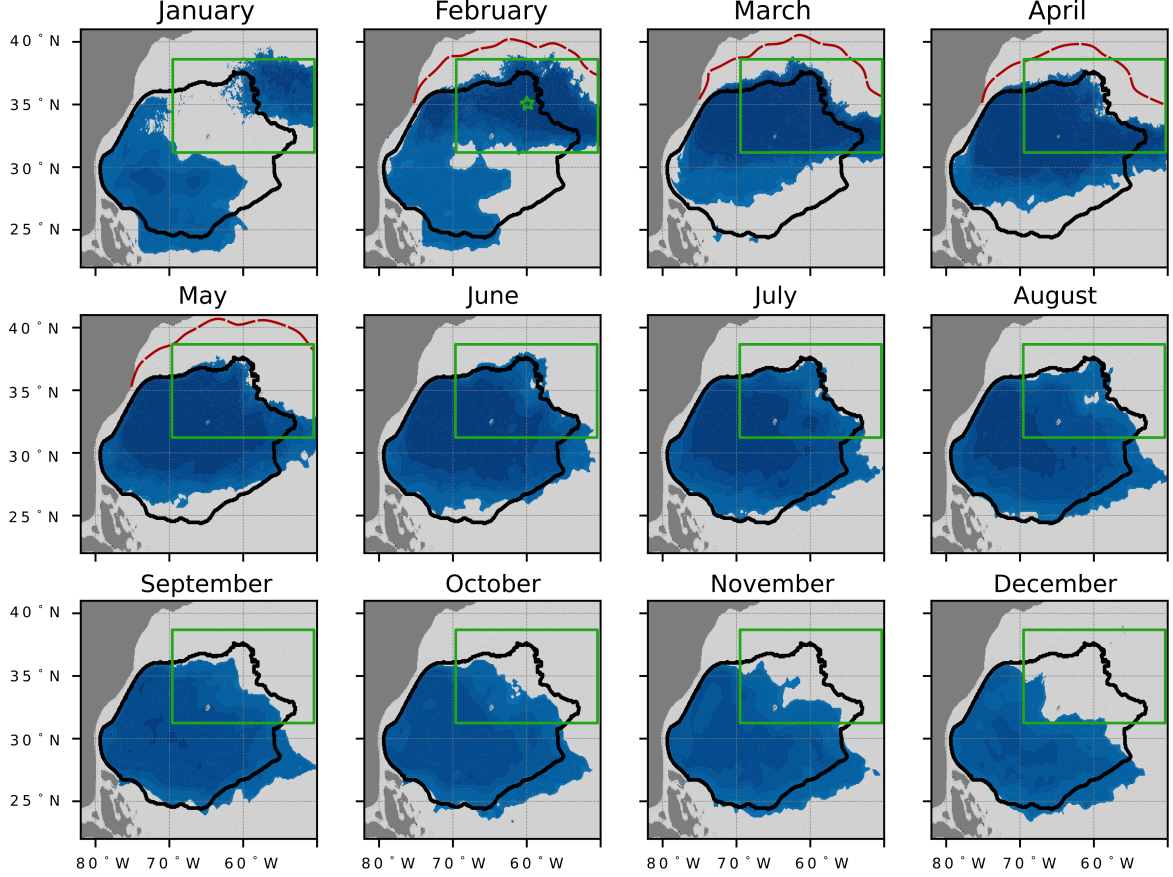


FIG. 5. Monthly-mean PV of STMW ($\overline{g^{-1}\Pi^{\#}} \leq 3 \times 10^{-10} \text{m}^{-1}\text{s}^{-1}$) on surface $\tilde{b} = -0.25 \text{ms}^{-2}$ appears and disappears during year 1967. Colors are given by the colorbar in Figure 4 (b). The lateral boundary C of the control volume Ω is determined by the annual-mean contour on $\overline{g^{-1}\Pi^{\#}} = 3 \times 10^{-10} \text{m}^{-1}\text{s}^{-1}$, and is plotted as the same black contour in each panel. Red dashed lines outline outcrops of this surface from February to May. ‘Formation zone’ bounded by the same green box in each panel is where low PV water is STMW’s formation and erosion phases, respectively. Green star located at 35°N , 60°W in February is where Warren (1972) determined the location of STMW formation.

qualitatively similar results, suggesting that the key features and conclusions of the study are not sensitive to the exact choice of the PV threshold (not shown).

4. Evolution of PV budget

In this section, we analyse the budget of the PV equation (20) integrated over the control volume Ω , which provides insights into the dynamics of STMW throughout the entire year 1967. The three-

dimensional integration over Ω is given by $\int d\Omega \stackrel{\text{def}}{=} \iiint_{\Omega} d\tilde{y} d\tilde{x} d\langle\sigma\rangle$. We apply this integration to equation (20) to investigate the PV dynamics. The temporal evolution of the volume of the control volume and the integrated PV are shown in panels (a) and (b) of Figure 6. Panel 6c shows the time series of the integrated terms from equation (20). The PV tendency $\Pi_{\tilde{r}}^{\#}$, plotted in light blue in panel 6d, is reproduced by summing up the other terms in (20).

A comparison between panels 6a and 6b shows that a decrease in PV within the STMW is associated with an increase in its volume, and vice versa. As the volume increases from February to early May, the PV decreases to its annual minimum. Subsequently, as the volume gradually declines, the PV slowly increases. These results confirm that the selected control volume in the core layer effectively captures the key characteristics of STMW formation and erosion.

Rewriting the $\hat{\mathbf{u}}$ -related terms in equation (20) gives

$$\int_{\Omega} [\nabla \cdot \mathbf{J}^{\#} - \Pi^{\#} \nabla \cdot \hat{\mathbf{u}}] d\Omega = \int_{\Omega} \hat{\mathbf{u}} \cdot (\Pi_{\tilde{x}}^{\#}, \Pi_{\tilde{y}}^{\#}, \Pi_{\tilde{b}}^{\#}) d\Omega. \quad (21)$$

The right-hand side of the equation, plotted in gray, can be interpreted as the net thickness transport into Ω along the direction of the non-thickness-weighted gradient of PV. Its temporal variation is consistent with that of the total thickness shown in panel (a), increasing from January to early May and gradually decreasing thereafter. The positive values indicate that $\hat{\mathbf{u}}$ and $(\Pi_{\tilde{x}}^{\#}, \Pi_{\tilde{y}}^{\#}, \Pi_{\tilde{b}}^{\#})$ are of the same signs, meaning that $\hat{\mathbf{u}}$ transports the volume up the PV gradient, leading to an increase in thickness inside the control volume. In other words, as the PV is transported outward by $\hat{\mathbf{u}}$, the volume is increased inwards.

After June, the diabatic velocity $\hat{\omega}$ is negligible as the outcropping migrates northwards. The TWA velocity divergence is persistently positive ($\nabla \cdot \hat{\mathbf{u}} > 0$), as shown by the difference between the gray and the pink lines. Consequently, $\langle\sigma\rangle^{-1} \langle\sigma\rangle_{\tilde{r}} = -\nabla \cdot \hat{\mathbf{u}} < 0$, and the layer thickness continuously reduces in time. This is consistent with the decreasing total thickness from June to November illustrated in Figures 3 and 6a.

Next, we investigate the role of the TWA velocity $\hat{\mathbf{u}}$ on the evolution of the integrated PV. As shown in panel (c) of Figure 6, the integrated divergence of the residual-mean PV flux (pink line), $\int_{\Omega} \nabla \cdot \mathbf{J}^{\#} d\Omega$, remains positive throughout the entire year. Based on the divergence theorem that the integrated divergence of a flux over a volume is equivalent to the net flux out of this volume,

342 this means that $\hat{\mathbf{u}}$ generally transports PV outward, leading to a PV extraction. This transport is
343 globally up the PV gradient, because the PV minimum is located within the control volume from
344 an annual-mean perspective. However, the direction does not always hold in time or space, which
345 will be further discussed in the following section.

346 The residual-eddy PV flux $\mathbf{F}^\#$ is along the lateral direction and does not cross \tilde{b} -surfaces. The
347 divergences of the E-P fluxes in $\mathbf{F}^\#$ accelerate/decelerate the lateral residual-mean flow (\hat{u}, \hat{v}) via
348 the lateral eddy momentum flux and the vertical eddy form stress (Stanley et al. 2020; Maddison
349 and Marshall 2013; Poulsen et al. 2019; Uchida et al. 2022). This eddy effect is reflected onto
350 the PV transport and is quantified by the divergence $\nabla \cdot \mathbf{F}^\#$, represented by the orange line in
351 panel 6c. The negative values of $\int_{\Omega} \nabla \cdot \mathbf{F}^\# d\Omega$ indicate that eddies tend to transport PV into the
352 control volume in an integrated sense. High PVs are transported down the gradient to mix with
353 low PVs, leading to an increase of PV inside the control volume.

354 The diabatic flux $\mathbf{G}^\#$ and its divergence are at least an order of magnitude smaller than those of
355 $\mathbf{J}^\#$ and $\mathbf{F}^\#$. The positive divergence (brown line) indicates that $\mathbf{G}^\#$ transports PV out of the control
356 volume, and is only noticeable during ventilation periods between February and May. The diabatic
357 impact on PV transport weakens significantly thereafter as the core layer in STMW is isolated from
358 the surface and subducted into the main thermocline, and contributes to an increase of PV in the
359 control volume from June to December, indicating a persistent PV diffusion through the cap of
360 STMW (Billheimer and Talley 2016).

361 The rate of PV change, shown in light blue in panel 6d, is reconstructed from the sum of the
362 divergences of the TWA velocity and PV fluxes. Its gradient is negative between January and
363 May, then changes sign with reduced magnitude thereafter, consistent with the evolution of the
364 integrated $\Pi^\#$ in panel 6b.

365 Overall, our results suggest that the evolution of the PV transport within the control volume is
366 dominated by the residual-mean PV flux, acting up the PV gradient in an integrated sense, and
367 is compensated by the down-gradient residual-eddy PV flux. This finding is consistent with the
368 results by Deremble and Dewar (2013). The effect of the diabatic PV flux is generally weaker than
369 that of the other two PV fluxes, but contributes to a decreasing PV during the formation period and
370 slightly increasing PV during the erosion period.

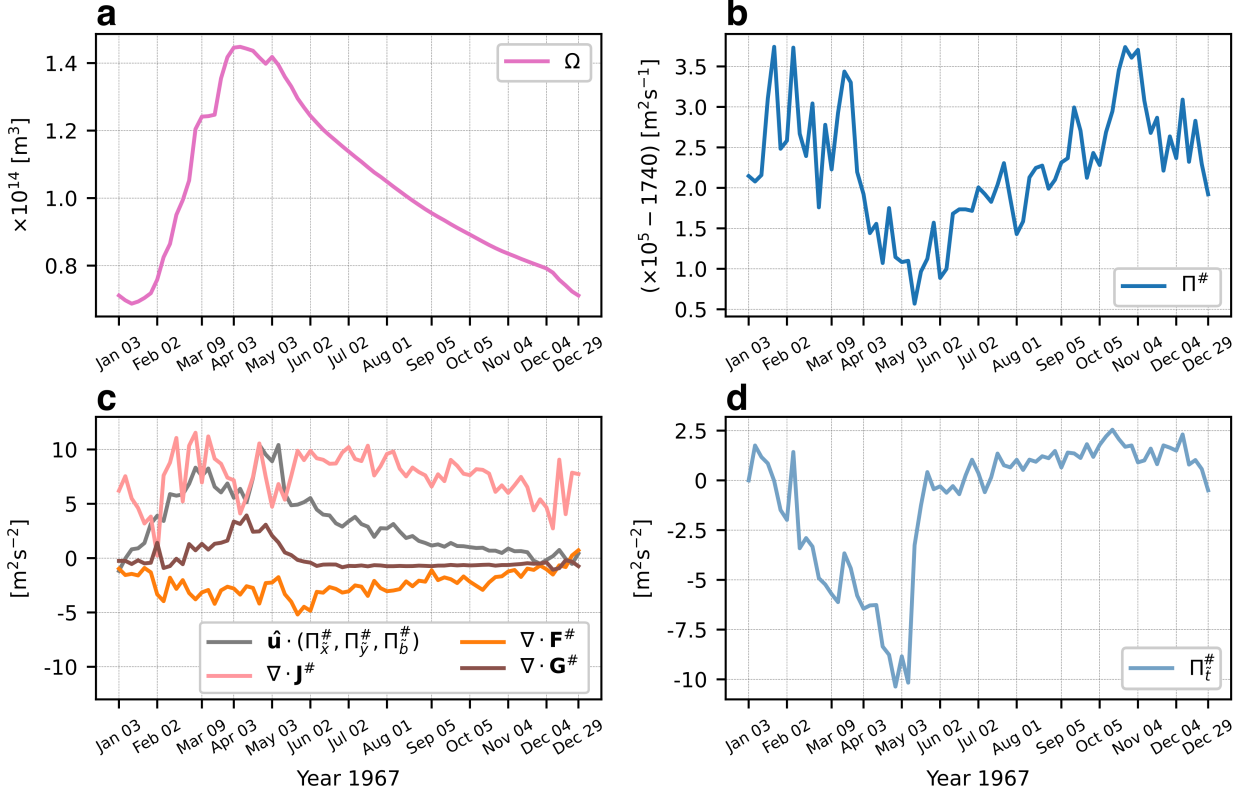


FIG. 6. Time series of integrated variables over the control volume Ω in the core layer. (a) Total volume $\int_{\Omega} dxdydz$; (b) Integrated PV $\int_{\Omega} \Pi^{\#} d\Omega$; (c) Integrated velocity weighted by the PV-gradient (gray), integrated divergences of the residual-mean PV flux (pink), the residual-eddy PV flux (orange), and the diabatic PV flux (brown); (d) Estimated tendency term reproduced by using the PV-gradient weighted velocity, the residual-eddy PV flux divergence and the diabatic PV flux divergence.

5. Regional mechanisms

In this section, we focus on the mean-eddy interactions and investigate the dynamical mechanisms of STMW maintenance in different regions in the North Atlantic. We approach it by examining the contribution of PV fluxes to the control volume from a spatial perspective. As the temporal variations of the residual-mean and residual-eddy PV fluxes do not exhibit obvious seasonality as discussed in Section 4, we are motivated to take an annual time-averaging of the integrated PV equation (20).

By assuming an adiabatic layer ($\hat{\omega} \sim 0$) in the annually averaged sense, we obtain

$$\int_{\Omega} \overline{\Pi_t^\#} d\Omega = - \int_{\Omega} \overline{-\Pi^\# \nabla_h \cdot \hat{\mathbf{u}}_h + \nabla_h \cdot \mathbf{J}_h^\# + \nabla_h \cdot \mathbf{F}^\# + \nabla_h \cdot \mathbf{G}_h^\#} d\Omega, \quad (22)$$

where the subscript h denotes the horizontal (lateral) components of the divergence operator and the fluxes. Residual-eddy PV flux $\mathbf{F}^\#$ is lateral by construction so does not have the subscript. Based on the divergence theorem, the volume integral on the RHS is equivalent to the sum of the fluxes across the lateral boundary surface \mathcal{S} of the control volume Ω .

$$\int_{\Omega} \overline{-\Pi^\# \nabla_h \cdot \hat{\mathbf{u}}_h + \nabla_h \cdot \mathbf{J}_h^\# + \nabla_h \cdot \mathbf{F}^\# + \nabla_h \cdot \mathbf{G}_h^\#} d\Omega = \int_{\mathcal{S}} \left[\overline{-\Pi^\# \hat{\mathbf{u}}_h} + \overline{\mathbf{J}_h^\#} + \overline{\mathbf{F}^\#} + \overline{\mathbf{G}_h^\#} \right] \cdot \mathbf{n} dS, \quad (23)$$

where \mathbf{n} is the outward-point normal unit vector on surface \mathcal{S} . Here, $\overline{\Pi^\#}$ is assumed to be nearly homogeneous within Ω , so that the volume integral of the PV-weighted divergence term $\overline{\Pi^\# \nabla_h \cdot \hat{\mathbf{u}}_h}$ can be approximated as $\nabla_h \cdot (\overline{\Pi^\# \hat{\mathbf{u}}_h})$ within Ω (light turquoise line). The lateral surface integral of the time-mean control volume is given by $\int_{\mathcal{S}} dS = \oint_C \overline{\langle \sigma \rangle} dl$, leading to

$$\int_{\mathcal{S}} \left[\overline{-\Pi^\# \hat{\mathbf{u}}_h} + \overline{\mathbf{J}_h^\#} + \overline{\mathbf{F}^\#} + \overline{\mathbf{G}_h^\#} \right] \cdot \mathbf{n} dS = \oint_C \left[\overline{-\langle \sigma \rangle \Pi^\# \hat{\mathbf{u}}_h} + \overline{\langle \sigma \rangle \mathbf{J}_h^\#} + \overline{\langle \sigma \rangle \mathbf{F}^\#} + \overline{\langle \sigma \rangle \mathbf{G}_h^\#} \right] \cdot \mathbf{n} dl, \quad (24)$$

where $\overline{\langle \sigma \rangle}$ is the annual-mean ensemble-mean layer thickness. Thus, the LHS of equation (22) can be expressed as a line integral of the sum of thickness-weighted fluxes along the closed (lateral) contour C (see black contours in Figure 4),

$$\int_{\Omega} \overline{\Pi_t^\#} d\Omega = - \oint_C \left[\overline{-\langle \sigma \rangle \Pi^\# \hat{\mathbf{u}}_h} + \overline{\langle \sigma \rangle \mathbf{J}_h^\#} + \overline{\langle \sigma \rangle \mathbf{F}^\#} + \overline{\langle \sigma \rangle \mathbf{G}_h^\#} \right] \cdot \mathbf{n} dl. \quad (25)$$

The thickness-weighted fluxes normal to the contour C are cumulatively integrated in a counter-clockwise direction in Figure 7. If, within a segment, the line gradient for a flux is positive then the flux transports PV out of the control volume. Since the annual mean PV is lower inside the control volume, an outward transport is directed up the PV gradient and indicates a PV extraction from STMW, and vice versa. The residual plotted in black is the RHS of equation (25), and represents an approximation of $\overline{\Pi_t^\#}$. Its line integral should ideally be continuous at p_1 since $\Pi^\#$ is expected to be

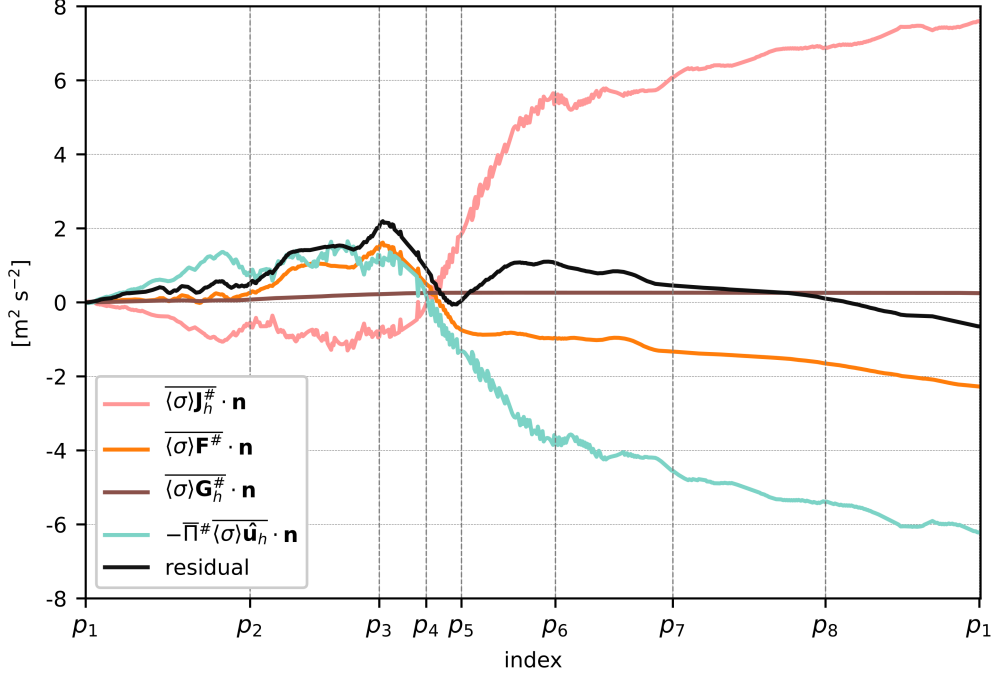


FIG. 7. Thickness-weighted PV fluxes are accumulated along the contour C from p_1 (see Figure 4b) in a counter-clockwise direction. Line colours used to represent the PV fluxes are consistent with those used in Figure 6. The unit vector \mathbf{n} along C points out of the control volume. Indices p_n 's are in correspondence with those labelled in Figure 4b, and are locations where the plotted terms change signs or strength. The PV-weighted TWA divergence is approximated by the contour integration of $\overline{\Pi^\#(\sigma)\hat{\mathbf{u}}_h \cdot \mathbf{n}}$, plotted in light turquoise. The residual term plotted in black is the sum of other lines, and is the estimation of the annual mean PV tendency, $\overline{\Pi_t^\#}$ which is expected to approach zero.

homogeneous within the control volume from a time-mean perspective. We attribute the observed discrepancy to unavoidable discretization errors, which will be discussed in detail in Section 7.

The contribution of the diabatic PV flux $\mathbf{G}^\#$ (brown line) is negligible since the layer is nearly adiabatic under an annual averaging. Thus, we focus on $\mathbf{F}^\#$ (orange line) and $\mathbf{J}^\#$ (pink line) and discuss their roles on PV transport in different regions. We label critical locations on the contour C by p -indices shown in Figure 4b, and split C into three segments as in the following subsections.

414 *a. Along-coast/Upstream of the Gulf Stream*

415 The most positive gradient is given by the residual-mean PV flux $\mathbf{J}^\#$ between locations p_6 and
416 p_3 . This segment of the contour follows the Florida current along the coast between 30°N and
417 35°N ($p_6 - p_5$) and then the upstream of GS after passing the separation point ($p_5 - p_3$). The result
418 suggests that the strongest PV extraction is due to $\mathbf{J}^\#$ and occurs in the boundary current region.
419 The underlying mechanism is that in this region the strong cross-jet flow intensifies the jet and
420 sharpens the PV gradients. The result here also suggests that the strength of the Florida current
421 as well as the upstream GS may be a key factor in determining the location of STMW, potentially
422 offering an explanation for its persistence throughout the year. Moreover, it may provide insight
423 into why mode water masses consistently form near western boundary currents (Hanawa and Talley
424 2001; Tsubouchi et al. 2016).

425 Along the same segment, the negative gradient of the accumulated residual-eddy PV flux $\mathbf{F}^\#$
426 suggests that $\mathbf{F}^\#$ transports PV down the gradient into the control volume. $\mathbf{F}^\#$ is relatively weak
427 between p_6 and p_5 as eddies play a secondary role along the coast. It becomes more prominent
428 between p_5 and p_3 since eddy activity is enhanced after the GS detaches from the coast near Cape
429 Hatteras.

430 *b. Northern Sargasso Sea*

431 The segment of contour between locations p_3 and p_1 lies in the northern Sargasso Sea and is south
432 of the GS, where STMW forms and erodes (Maze et al. 2013; Billheimer and Talley 2016). Along
433 this segment, both the residual-mean and residual-eddy PV fluxes reverse their directions in terms
434 of transporting the PV compared to those in the upstream (subsection *a*). $\mathbf{F}^\#$ transports PV out
435 of the control volume, approximately northward, whereas $\mathbf{J}^\#$ transports PV inside, approximately
436 southward. This is because mean-eddy interactions exhibit distinct mechanisms in the along-coast
437 region, near the separation point, and in the meandering region (Waterman and Hoskins 2013;
438 Kang and Curchitser 2015).

439 From an annual-mean perspective, in this region, the residual-eddy flux $\mathbf{F}^\#$ contributes to a
440 decrease of PV within the control volume, indicating a formation of STMW, and the residual-mean
441 flux $\mathbf{J}^\#$ contributes to an increase of PV, indicating an erosion of STMW. However, this is not true
442 when low PV water is formed in early winter and migrates southward into the control volume (see

panels for January and February in Figure 5). During this period, $\mathbf{J}^\#$, acting up the PV gradient, transports the newly formed low PV water into the control volume, and $\mathbf{F}^\#$ mixes this low PV water with the existing PV pool in a downgradient direction. This means that both the formation and erosion of STMW occurring in the Southern GS flank/northern Sargasso Sea is mainly driven by the residual-mean PV flux, and this transport is always balanced by the counteracting residual eddy PV transport.

Overall, our results suggest that STMW's annual cycle is highly correlation to the path and strength of the GS, consistent with previous findings (Stevens et al. 2020; Joyce et al. 2000; Tsubouchi et al. 2016).

c. Southern Sargasso Sea

Indices p_1 to p_6 in a clockwise direction along the contour trace the recirculation path of the subtropical gyre. Along this segment of the contour, the extraction of PV by $\mathbf{J}^\#$ progressively weakens. A similar finding is reported in Billheimer and Talley (2016), who showed that the destruction rate of STMW is weaker in the southern Sargasso Sea than in the GS region. Although the residual-eddy PV flux $\mathbf{F}^\#$ is weaker in magnitude than its mean counterpart $\mathbf{J}^\#$ (their spatial fields not shown), its contribution to PV transport is comparable. This is evident when comparing the slopes of the pink and orange lines between locations p_6 and p_1 . Because $\mathbf{F}^\#$ tends to align more closely with \mathbf{n} , the residual eddies transport PV down the gradient and erode STMW more effectively.

6. Role of bolus transport on STMW formation

We have demonstrated in previous sections that the eddy effects on PV transport quantified by the residual-eddy PV flux $\mathbf{J}^\#$ exhibit little temporal variations annually. In this section, we investigate eddy PV transport by the bolus eddy velocity and its relation to STMW formation.

We recall that since the lateral TWA velocity $\hat{\mathbf{u}}_h$ and the lateral ensemble-mean velocity $\langle \mathbf{u} \rangle_h$ are related via a bolus velocity \mathbf{u}^* defined as (17), the lateral residual-mean PV flux can be decomposed into a lateral ensemble-mean PV flux and a bolus PV flux, respectively,

$$\mathbf{J}_h^\# = \langle \mathbf{u} \rangle_h \Pi^\# + \mathbf{u}^* \Pi^\#. \quad (26)$$

The bolus PV flux $\mathbf{u}^*\Pi^\#$ quantifies the lateral eddy advection of PV due to thickness variations.

Figure 8 illustrates the monthly fields of the magnitudes of the bolus PV flux. Starting in February, $\mathbf{u}^*\Pi^\#$ begins to emerge in the Northern Sargasso Sea, with the strongest signals observed between 30°N and 35°N (outlined by white dashed lines). This region corresponds to where observation-based studies have detected STMW formation during winter (Maze et al. 2009; Billheimer and Talley 2016), and overlaps with the "formation zone" of the simulated STMW identified in our study (indicated by green boxes in Figure 5).

From July onward, the magnitude of the bolus PV flux declines sharply within the control volume, as the layer thickness is much more uniform. To further investigate, we compare the strength and direction of the ensemble-mean PV flux and the bolus eddy PV flux during two periods—February to June and July to November—in Figure 9. We find that the bolus eddy flux is at least an order of magnitude weaker than the ensemble-mean PV flux and generally transports PV in the opposite direction within the control volume.

Between February and June, the thickness of the core layer within the "formation zone" increases significantly, as indicated by the vertical displacement of the red slope between 30°N and 35°N in Figure 3, leading to enhanced baroclinic instability. As a consequence, an intensified northeastward bolus eddy transport of thickness and PV is observed between 28°N and 36°N in Figure 9, and partially cancels out the southwestward transport associated with $\langle \mathbf{u}_h \rangle$. Between July and November, the bolus PV flux becomes negligible compared to its ensemble-mean counterpart, and the opposing transport directions of the two fluxes are no longer clearly observed.

This time-dependent mean-eddy interaction offers insight into the mechanisms of lateral eddy mixing in STMW formation, which has been identified as crucial in the northern Sargasso Sea near the GS (Billheimer and Talley 2016). Specifically, newly formed low PV water, generated by surface buoyancy loss, is advected southward into the western Sargasso Sea by the large-scale ensemble-mean flow $\langle \mathbf{u}_h \rangle$. It is then actively mixed with pre-existing low PV water via an eddy-induced bolus transport, until the PV field in region, that is, the control volume in our study, is well-mixed (Marshall et al. 1999). An analogy of this can be found for the Deacon cell in the Southern Ocean; the upwelling water in isopycnal layers and northward transport by Ekman pumping is counteracted by an bolus-driven overturning (Abernathey et al. 2011; Marshall and Speer 2012).

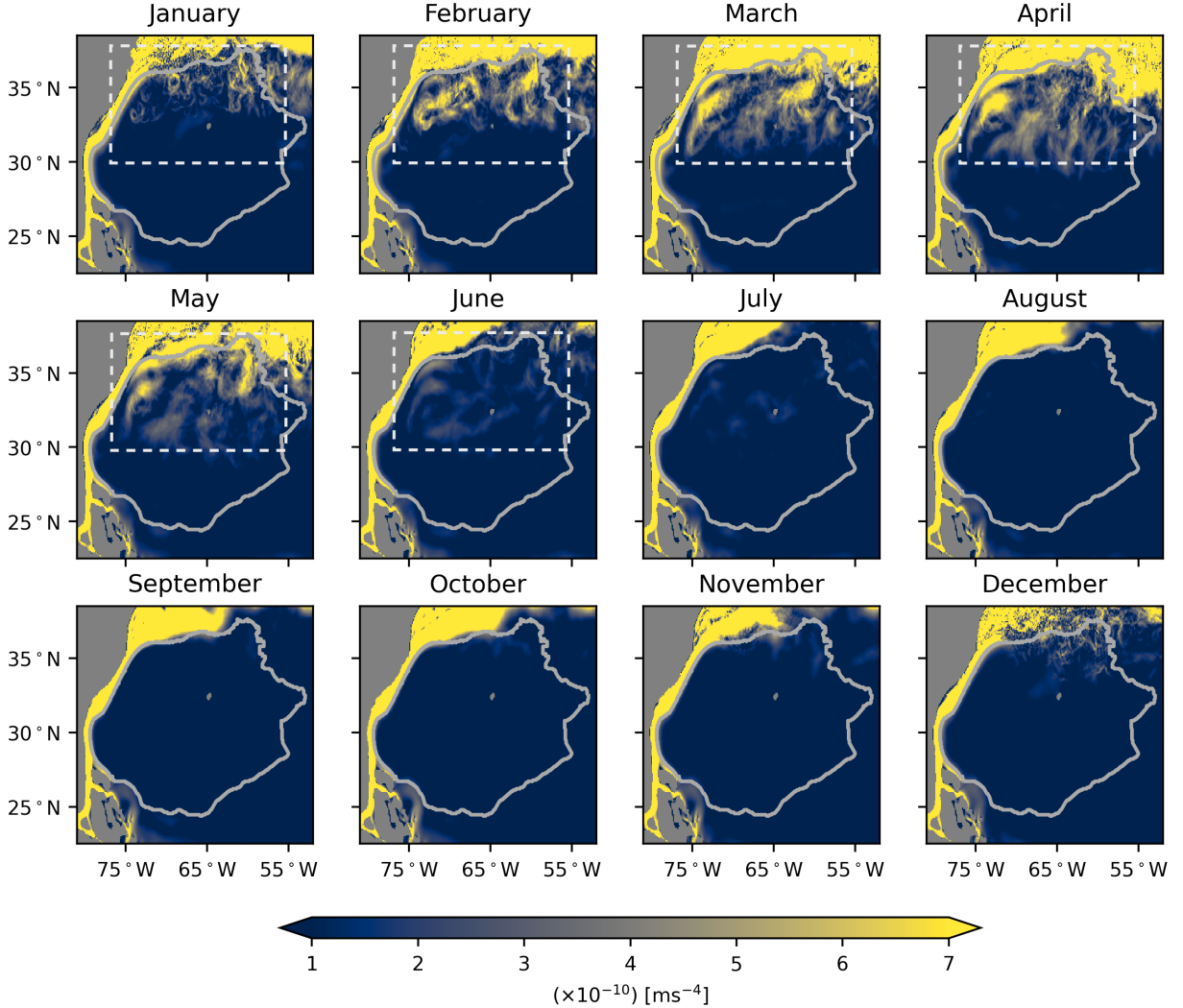


FIG. 8. Magnitudes of the monthly-mean bolus PV flux $||\mathbf{u}^* \Pi^{\#}||$ on surface $\tilde{b} = -0.25 \text{ m s}^{-2}$ in the core layer. Gray contour in each panel is the lateral boundary C of the control volume Ω . Between February and June, the region where the core layer is thickened due to ventilation is outlined by the same white dashed frame. The bolus PV flux inside this region is enhanced significantly in magnitudes due to the intensified baroclinic instability.

7. Discussion

Before concluding, we discuss the numerical accuracy of our methodology and the challenges associated with closing the TWA PV budget within the control volume Ω . Given that we cannot diagnose the ‘true’ tendency of PV using instantaneous snapshot outputs every five days, the reproduced PV tendency (Figure 6d) does not exactly align with the offline temporal derivative

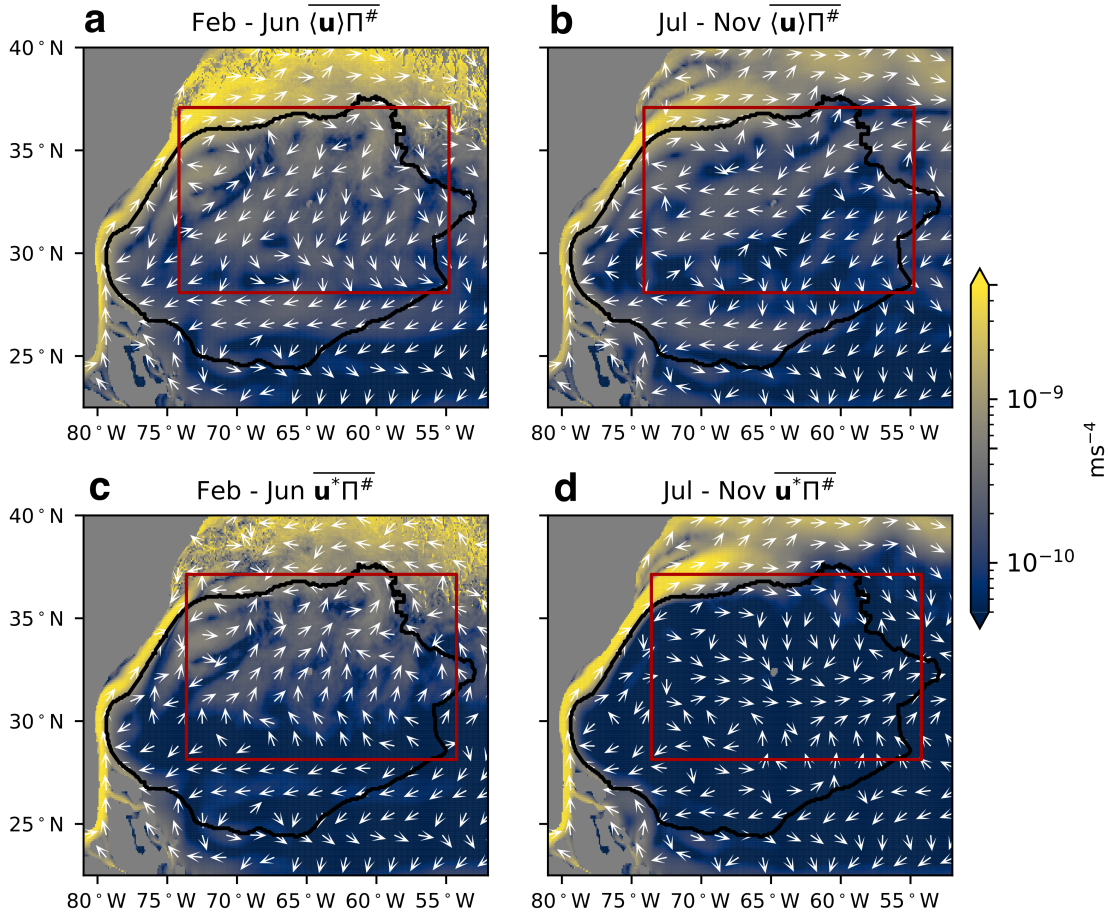


FIG. 9. Time-mean fields of the lateral ensemble-mean PV flux and the bolus PV flux between (a,b) February and June, and (c,d) between July and November. The region where the bolus PV flux intensifies/weakens and is of opposite directions of the ensemble-mean PV flux is outlined by the red frame in each panel.

of PV in Figure 6b. We attribute this discrepancy to technical challenges in implementing the TWA framework and determining a time-varying control volume (Stanley and Marshall 2022), and temporal aliasing. We outline some of the technical caveats below.

The residual-mean momentum equations and the thickness equation in (7) cannot be closed to numerical precision in an offline diagnostics due to the non-commutability between the TWA operator and space-time gradients, and hence, neither can the PV equation. This is because the layer thickness σ is precisely defined to be spatially and temporally dependent in z -coordinates. When transforming a thickness-weighted variable from z -coordinates to \tilde{b} -coordinates, this precision on σ is lost, and discretization errors accumulate in the computations. For example, even though the

divergence operator ∇ is theoretically coordinate-invariant, numerical errors induced by applying the formulation (12) are non-negligible and they further result in a biased integration of $\Pi_i^\#$. This sensitivity of TWA and thickness equation to offline vertical coordinate transformation has also been reported by Stanley and Marshall (2022).

Furthermore, it is essential to retain the ventilated portion of STMW (Billheimer and Talley 2013, 2016; Maze et al. 2013; Li et al. 2022) to ensure that diabatic effects on STWM formation are captured. However, this introduces two sources of errors in estimating the PV budget within Ω . The accuracy of the methodology will be less promising over the corresponding periods since the buoyancy coordinate becomes increasingly ill-defined in the mixed layer, and $d\tilde{b}$ and $d\zeta$ in (2) approach zero towards the surface. We suspect that a better budget closure may be achieved if a layer exhibiting less spatial and temporal variabilities than ours in $\langle\sigma\rangle$ is considered, which does not exist within STWM, and/or if TWA diagnostics are computed online (cf. Ferreira and Marshall 2006; Ringler et al. 2017).

Despite these caveats, we argue that the crucial dynamics of PV evolution are well represented by the governing terms in equation (20), besides numerical inaccuracies. In Figure 6, $\Pi_i^\#$ reconstructed by these terms follows the same trend as the integrated $\Pi^\#$, and both capture the annual cycle of STMW formation and erosion. As discussed in previous sections, we have demonstrated that the contribution of the governing terms to the PV evolution is consistent with previous theoretical studies (Dewar 1986; Deremble and Dewar 2013).

8. Conclusions

In this study, we have investigated the primary mechanisms governing the maintenance of Subtropical Mode Water (STMW) in the North Atlantic. We have focused on the interactions between the mean flow and eddies, and their impacts on the annual life cycle of STMW. We have used an ensemble of 48 partially air-sea coupled North Atlantic simulations at $1/12^\circ$ resolution. This ensemble approach permits a separation of eddies from a full flow without prescribing any temporal or spatial scale. As both eddies and ensemble-mean variables are spatial and temporally dependent, we were able to explore their full impacts on the dynamics of STMW's annual evolution. By implementing a thickness-weighted averaging (TWA) framework, we have formulated a potential vorticity (PV) equation for $\Pi^\#$ in buoyancy layers, analogous to the flux-form

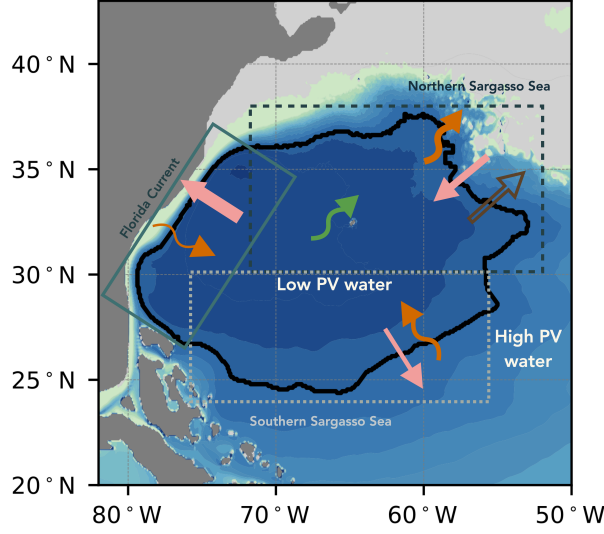


FIG. 10. Schematic illustration of the dynamical mechanisms maintaining the Subtropical Mode Water (STMW) in the North Atlantic. The background shading shows the annual-mean PV $\overline{\Pi^\#}$, with darker blue indicating lower PV values. The black contour outlines the low PV pool characterising STMW in its core layer. Distinct mechanisms are found in the three regions outlined with different line styles. Within these regions, pink arrows denote the residual-mean PV flux, and orange curved arrows denote the residual-eddy PV flux. Arrow direction indicates the net direction of PV transport, while arrow thickness indicates relative flux magnitude. In the northern Sargasso Sea region, a brown outlined arrow denotes the diabatic PV flux, and a green curved arrow denotes the bolus PV flux; both are active primarily during the formation phase.

Ertel's PV equation. To quantify the dynamics of STMW, we have studied the budget of a low PV pool enclosed by a control volume Ω in the core STMW layer.

Our results highlight that the annual life cycle of STMW is primarily determined by the residual-mean flow, represented by the TWA velocity $\hat{\mathbf{u}}$, whereas the eddy and diabatic forcing play a secondary role. The thickness-weighted ensemble-mean velocity $\hat{\mathbf{u}}$ governs the conservation of the ensemble-mean thickness $\langle \sigma \rangle$ within buoyancy layers. It drives an increase in $\langle \sigma \rangle$ within the control volume between February and May, corresponding to the formation phase of STMW, and a subsequent decrease thereafter, consistent with its erosion phase. On the other hand, the associated residual-mean PV flux $\mathbf{J}^\#$ does not exhibit a pronounced seasonal variability. In an integrated and annually-averaged sense, $\mathbf{J}^\#$ extracts PV from the control volume through an upgradient advection.

567 The strongest outward PV flux occurs along the coastline, where the PV gradient is the sharpest,
568 and follows the Gulf Stream until the separation point (29°N to 36°N). This persistent extraction
569 of PV throughout the year may provide an explanation for the existence of STMW in the western
570 Sargasso Sea, as well as for the consistent presence of mode waters adjacent to western boundary
571 currents.

572 Eddy effects are partially embedded within the residual-mean PV flux, capturing the lateral
573 advection of PV by bolus eddies. Our results show that the bolus eddy transport is strongly
574 linked to the STMW formation phase. The bolus PV flux, $\mathbf{u}^*\Pi^\#$, intensifies within the control
575 volume between February and June, coinciding with the thickening of the core layer due to surface
576 ventilation. As newly formed low-PV water north of the Gulf Stream is advected into the Sargasso
577 Sea by the ensemble-mean PV flux $\langle \mathbf{u}_h \rangle \Pi^\#$, the bolus PV flux associated with the variation of
578 the layer thickness mixes it with pre-existing low-PV water in the control volume by counteracting
579 the ensemble-mean PV flux. This eddy-mean counteraction flattens the tilted buoyancy layers
580 and leads to a nearly homogeneous PV field within the control volume. Since the residual-mean
581 velocity inherently represents the cancellation between the bolus and ensemble-mean velocities,
582 seasonal variations driven by the bolus eddy transport are not directly reflected in the temporal
583 evolution of the residual-mean PV flux.

584 The eddy forcing in the PV equation is represented by the residual-eddy PV flux $\mathbf{F}^\#$, which
585 quantifies the effects of residual eddy momentum fluxes and vertical eddy form stress on PV
586 transport. The divergence of $\mathbf{F}^\#$ is approximately one order of magnitude smaller than that of its
587 residual-mean counterpart, $\mathbf{F}^\#$. Despite that, $\mathbf{F}^\#$ plays a crucial role in the PV evolution within
588 the control volume, and thus in the STMW's life cycle, since it consistently acts to counterbalance
589 the transport by $\mathbf{J}^\#$. The integrated residual-eddy PV flux $\mathbf{F}^\#$ over the control volume does not
590 exhibit strong seasonality, similar to the residual-mean PV flux $\mathbf{J}^\#$, but it tends to transport PV
591 down the gradient, resulting in a net increase of PV within the control volume. This behavior,
592 as well as that by the bolus eddy PV flux, is consistent with the classical assumption of down-
593 gradient eddy transport (Green 1970; Rhines and Young 1982). To rigorously determine whether
594 eddy mixing—whether by residual eddies or bolus eddies—acts down-gradient or up-gradient in
595 a full spatio-temporal sense, it would be necessary to explicitly compute the eddy diffusivity (e.g.
596 Bachman et al. 2020; Haigh et al. 2021; Uchida et al. 2023). This question remains important,

597 especially given that many mesoscale eddy parameterizations, such as the Gent-McWilliams' skew
598 diffusion (GM; Gent and McWilliams 1990; Griffies 2018) and its extensions (e.g. Treguier et al.
599 1997; Aiki et al. 2004; Cessi 2008; Marshall et al. 2012; Mak et al. 2023), are developed based on
600 the assumption of down-gradient eddy transport.

601 We have diagnosed the spatial contributions of the residual-mean and residual-eddy PV fluxes by
602 calculating their net fluxes along different segments of the lateral contour in an annually averaged
603 sense. The contribution of the diabatic PV flux $\mathbf{G}^\#$ is found to be small, as the buoyancy layer is
604 nearly adiabatic when averaged over the year; nevertheless, their contribution become noticeable
605 during late winter when the layers outcrop at the surface. Along the coastal segment, eddy effects
606 are secondary because the strong Gulf Stream jet inhibits significant eddy generation. In contrast,
607 the contribution of $\mathbf{F}^\#$ becomes most pronounced along the northern boundary of the control
608 volume, situated on the southern flank of the Gulf Stream, where eddy activity intensifies after the
609 Gulf Stream detaches from the coast. This result stresses the importance of eddy effects in both the
610 formation and erosion of STMW, as this region is critical for the initiation of its annual renewal and
611 decay. In the southern Sargasso Sea, following the recirculation pathway of the subtropical gyre, the
612 PV transport is approximately balanced between the residual-mean and residual-eddy fluxes. This
613 finding suggests that, even though eddies are relatively weak in this region, their contribution to the
614 maintenance of STMW is nonetheless substantial. Overall, the interaction between the residual-
615 mean flow and residual-eddies, and consequently their impacts on PV transport, as summarized in
616 Figure 10, varies significantly in space and time, giving rise to a complex and regionally dependent
617 mechanism governing the formation, erosion and maintenance of STMW.

618 Our work highlights a unique advantage of the ensemble approach, which enables probing into
619 the full spatiotemporal effects of bolus eddies in western boundary current extensions. In contrast
620 to the Southern Ocean, where zonal-mean analyses of the residual-mean flow are commonly
621 employed, the presence of lateral boundaries in the North Atlantic precludes such an approach.
622 Our results, together with previous studies on the Antarctic Circumpolar Current (e.g. Marshall
623 and Radko 2003; Abernathey et al. 2011; Sinha and Abernathey 2016; Bishop et al. 2016, and
624 references therein), suggest that the partial cancellation between the Eulerian-mean and bolus-eddy
625 flows is a ubiquitous feature of oceanic jets.

Acknowledgments. We dedicate this study in memory of Prof. William K. Dewar, with deep respect. L. Sun is especially grateful for his mentorship — his intellectual guidance and unwavering support were instrumental throughout the development of this work. W. Dewar was supported through National Science Foundation (NSF) grants OCE-1829856, OCE-1941963, OCE-2023585, and OCE-2123632, and the French ‘Make Our Planet Great Again’ (MOPGA) program managed by the Agence Nationale de la Recherche under the Programme d’Investissement d’Avenir, reference ANR-18-MPGA-0002. L. Sun acknowledges support by the latter two grants. T. Uchida acknowledges the NASA award 80NSSC24K1649. A. Poje acknowledges support from the NSF grant OCE-2123633. High-performance computing resources on Cheyenne (doi : 10.5065/D6RX99HX) used for running the Chaocean ensemble of the North Atlantic were provided by NCAR’s Computational and Information Systems Laboratory, sponsored by NSF, under the university large allocation UFSU0011. We are grateful to Qian Li and Yueyang Lu for their insightful discussions. We would like to extend our gratitude to Edward Peirce and Kelly Hirai for maintaining the FSU cluster on which the data were analyzed.

Data availability statement. EN.4.2.2 data were obtained from <https://www.metoffice.gov.uk/hadobs/en4/> and are © British Crown Copyright, Met Office, 2013, provided under a Non-Commercial Government Licence (<http://www.nationalarchives.gov.uk/doc/non-commercial-government-licence/version/2/>; Good et al. 2013). The NA12 ensemble outputs are available via the Florida State University (FSU) cluster (http://ocean.fsu.edu/~qjamat/share/data/twa_Uchida/).

References

- Abernathey, R., J. Marshall, and D. Ferreira, 2011: The dependence of Southern Ocean meridional overturning on wind stress. *Journal of Physical Oceanography*, **41** (12), 2261–2278, <https://doi.org/10.1175/JPO-D-11-023.1>.
- Aiki, H., T. Jacobson, and T. Yamagata, 2004: Parameterizing ocean eddy transports from surface to bottom. *Geophysical research letters*, **31** (19), <https://doi.org/10.1029/2004GL020703>.
- Aoki, K., 2014: A constraint on the thickness-weighted average equation of motion deduced from energetics. *Journal of Marine Research*, **72**, 355–382, URL <https://elischolar.library.yale.edu/>

cgi/viewcontent.cgi?article=1396&context=journal_of_marine_research.

Bachman, S. D., B. Fox-Kemper, and F. O. Bryan, 2020: A Diagnosis of Anisotropic Eddy Diffusion From a High-Resolution Global Ocean Model. *Journal of Advances in Modeling Earth Systems*, **12** (2), <https://doi.org/10.1029/2019MS001904>.

Billheimer, S., and L. D. Talley, 2013: Near cessation of Eighteen Degree Water renewal in the western North Atlantic in the warm winter of 2011–2012. *Journal of Geophysical Research: Oceans*, **118** (12), 6838–6853, <https://doi.org/10.1002/2013JC009024>.

Billheimer, S., and L. D. Talley, 2016: Annual cycle and destruction of Eighteen Degree Water. *J. Geophys. Res. Oceans*, **121** (9), 6604–6617, <https://doi.org/10.1002/2016JC011799>.

Bishop, S. P., P. R. Gent, F. O. Bryan, A. F. Thompson, M. C. Long, and R. P. Abernathey, 2016: Southern Ocean overturning compensation in an eddy-resolving climate simulation. *Journal of Physical Oceanography*, **46** (5), 1575–1592, <https://doi.org/10.1175/JPO-D-15-0177.1>.

Cessi, P., 2008: An energy-constrained parameterization of eddy buoyancy flux. *Journal of Physical Oceanography*, **38** (8), 1807–1819, <https://doi.org/10.1175/2007JPO3812.1>.

Cheng, L., J. Zhu, R. Cowley, T. Boyer, and S. Wijffels, 2014: Time, probe type, and temperature variable bias corrections to historical expendable bathythermograph observation. *Journal of Atmospheric and Oceanic Technology*, **31** (08), <https://doi.org/10.1175/JTECH-D-13-00197.1>.

Constantinou, N. C., and A. M. Hogg, 2021: Intrinsic oceanic decadal variability of upper-ocean heat content. *Journal of Climate*, **34** (15), 6175–6189, <https://doi.org/10.1175/JCLI-D-20-0774.1>.

Czaja, A., and U. Hausmann, 2009: Observations of Entry and Exit of Potential Vorticity at the Sea Surface. *Journal of Physical Oceanography*, **39**, <https://doi.org/10.1175/2009JPO4024.1>.

de Boyer Montégut, C., G. Madec, A. S. Fischer, A. Lazar, and D. Iudicone, 2004: Mixed layer depth over the global ocean: An examination of profile data and a profile-based climatology. *Journal of Geophysical Research: Oceans*, **109** (C12), <https://doi.org/10.1029/2004JC002378>.

- Deremble, B., and W. K. Dewar, 2013: Volume and Potential Vorticity Budgets of Eighteen Degree Water. *Journal of Physical Oceanography*, **43** (11), 2309–2321, <https://doi.org/10.1175/JPO-D-13-052.1>.
- Deremble, B., N. Wienders, and W. K. Dewar, 2013: CheapAML: A simple, atmospheric boundary layer model for use in ocean-only model calculations. *Monthly Weather Review*, **141** (2), 809–821, <https://doi.org/10.1175/MWR-D-11-00254.1>.
- Dewar, W. K., 1986: On the Potential Vorticity Structure of Weakly Ventilated Isopycnals: A Theory of Subtropical Mode Water Maintenance. *Journal of Physical Oceanography*, **16** (7), 1204–1216, [https://doi.org/10.1175/1520-0485\(1986\)016<1204:OTPVSO>2.0.CO;2](https://doi.org/10.1175/1520-0485(1986)016<1204:OTPVSO>2.0.CO;2).
- Ferreira, D., and J. Marshall, 2006: Formulation and implementation of a “residual-mean” ocean circulation model. *Ocean Modelling*, **13** (1), 86–107, <https://doi.org/10.1016/j.ocemod.2005.12.001>.
- Forget, G., 2010: Mapping ocean observations in a dynamical framework: A 2004–06 ocean atlas. *Journal of Physical Oceanography*, **40** (6), 1201–1221, <https://doi.org/10.1175/2009JPO4043.1>.
- Forget, G., G. Maze, M. Buckley, and J. Marshall, 2011: Estimated Seasonal Cycle of North Atlantic Eighteen Degree Water Volume. *Journal of Physical Oceanography*, **41** (2), 269–286, <https://doi.org/10.1175/2010JPO4257.1>.
- Gent, P. R., and J. C. McWilliams, 1990: Isopycnal Mixing in Ocean Circulation Models. *Journal of Physical Oceanography*, **20** (1), 150–155, [https://doi.org/10.1175/1520-0485\(1990\)020<0150:IMIOCM>2.0.CO;2](https://doi.org/10.1175/1520-0485(1990)020<0150:IMIOCM>2.0.CO;2).
- Good, S. A., M. J. Martin, and N. A. Rayner, 2013: EN4: Quality controlled ocean temperature and salinity profiles and monthly objective analyses with uncertainty estimates. *Journal of Geophysical Research: Oceans*, **118** (12), 6704–6716, <https://doi.org/10.1002/2013JC009067>.
- Green, J. S. A., 1970: Transfer properties of the large-scale eddies and the general circulation of the atmosphere. *Quarterly Journal of the Royal Meteorological Society*, **96** (408), 157–185, <https://doi.org/10.1002/qj.49709640802>.
- Griffies, S. M., 2018: *Fundamentals of ocean climate models*. Princeton university press.

707 Haigh, M., L. Sun, J. C. McWilliams, and P. Berloff, 2021: On eddy transport in the ocean. Part
 708 I: The diffusion tensor. *Ocean Modelling*, **164**, 101–831, [https://doi.org/10.1016/j.ocemod.2021.](https://doi.org/10.1016/j.ocemod.2021.101831)
 709 101831.

710 Hanawa, K., and L. D. Talley, 2001: Mode waters. *International geophysics*, Vol. 77, Elsevier,
 711 373–386.

712 Haynes, P. H., and M. E. McIntyre, 1987: On the Evolution of Vorticity and Potential Vorticity
 713 in the Presence of Diabatic Heating and Frictional or Other Forces. *Journal of the Atmospheric*
 714 *Sciences*, **44** (5), 828–841, [https://doi.org/10.1175/1520-0469\(1987\)044<0828:OTEOVA>2.0.](https://doi.org/10.1175/1520-0469(1987)044<0828:OTEOVA>2.0.CO;2)
 715 CO;2.

716 Jamet, Q., W. K. Dewar, N. Wienders, and B. Deremble, 2019: Spatiotemporal Patterns of Chaos
 717 in the Atlantic Overturning Circulation. *Geophysical Research Letters*, **46** (13), 7509–7517,
 718 <https://doi.org/10.1029/2019GL082552>.

719 Jamet, Q., W. K. Dewar, N. Wienders, B. Deremble, S. Close, and T. Penduff, 2020: Locally and
 720 remotely forced subtropical AMOC variability: A matter of time scales. *Journal of Climate*,
 721 **33** (12), 5155–5172, <https://doi.org/10.1175/jcli-d-19-0844.1>.

722 Joyce, T. M., 2013: New perspectives on eighteen-degree water formation in the north atlantic. *New*
 723 *Developments in Mode-Water Research: Dynamic and Climatic Effects*, 41–48, [https://doi.org/](https://doi.org/10.1007/978-4-431-54162-2_3)
 724 10.1007/978-4-431-54162-2_3.

725 Joyce, T. M., C. Deser, and M. A. Spall, 2000: The Relation between Decadal Variability of
 726 Subtropical Mode Water and the North Atlantic Oscillation. *Journal of Climate*, **13** (14), 2550–
 727 2569, [https://doi.org/10.1175/1520-0442\(2000\)013<2550:TRBDVO>2.0.CO;2](https://doi.org/10.1175/1520-0442(2000)013<2550:TRBDVO>2.0.CO;2).

728 Joyce, T. M., L. N. Thomas, W. K. Dewar, and J. B. Girtton, 2013: Eighteen Degree Water
 729 formation within the Gulf Stream during CLIMODE. *Deep Sea Research Part II: Topical*
 730 *Studies in Oceanography*, **91**, 1–10, <https://doi.org/10.1016/j.dsr2.2013.02.019>.

731 Kang, D., and E. N. Curchitser, 2015: Energetics of eddy–mean flow interactions in the gulf
 732 stream region. *Journal of Physical Oceanography*, **45** (4), 1103–1120, [https://doi.org/10.1175/](https://doi.org/10.1175/JPO-D-14-0156.1)
 733 JPO-D-14-0156.1.

734 Kwon, Y.-O., and S. C. Riser, 2004: North Atlantic Subtropical Mode Water: A history of
 735 ocean-atmosphere interaction 1961–2000. *Geophysical Research Letters*, **31** (19), [https://doi.org/](https://doi.org/10.1029/2004GL021116)
 736 10.1029/2004GL021116.

737 Leroux, S., T. Penduff, L. Bessi eres, J.-M. Molines, J.-M. Brankart, G. S erazin, and Coau-
 738 thors, 2018: Intrinsic and atmospherically forced variability of the amoc: Insights from
 739 a large-ensemble ocean hindcast. *Journal of Climate*, **31** (3), 1183–1203, [https://doi.org/](https://doi.org/10.1175/JCLI-D-17-0163.1)
 740 10.1175/JCLI-D-17-0163.1.

741 Li, K., G. Maze, and H. Mercier, 2022: Ekman Transport as the Driver of Extreme Interannual
 742 Formation Rates of Eighteen Degree Water. *Journal of Geophysical Research: Oceans*, **127** (1),
 743 <https://doi.org/10.1029/2021JC017696>.

744 Luyten, J. R., J. Pedlosky, and H. Stommel, 1983: The Ventilated Thermocline. *Journal of*
 745 *Physical Oceanography*, **13** (2), 292–309, [https://doi.org/10.1175/1520-0485\(1983\)013<0292:](https://doi.org/10.1175/1520-0485(1983)013<0292:TVT>2.0.CO;2)
 746 TVT>2.0.CO;2.

747 Maddison, J. R., and D. P. Marshall, 2013: The Eliassen–Palm flux tensor. *Journal of Fluid*
 748 *Mechanics*, **729**, 69–102, <https://doi.org/10.1017/jfm.2013.259>.

749 Mak, J., J. R. Maddison, D. P. Marshall, X. Ruan, Y. Wang, and L. Yeow, 2023: Scale-awareness in
 750 an eddy energy constrained mesoscale eddy parameterization. *Journal of Advances in Modeling*
 751 *Earth Systems*, **15** (12), e2023MS003 886, <https://doi.org/10.1029/2023MS003886>.

752 Marshall, D. P., J. R. Maddison, and P. S. Berloff, 2012: A Framework for Parameterizing Eddy
 753 Potential Vorticity Fluxes. *Journal of Physical Oceanography*, **42** (4), 539–557, [https://doi.org/](https://doi.org/10.1175/JPO-D-11-048.1)
 754 10.1175/JPO-D-11-048.1.

755 Marshall, D. P., R. G. Williams, and M. M. Lee, 1999: The relation between eddy-induced transport
 756 and isopycnic gradients of potential vorticity. *Journal of Physical Oceanography*, **29** (7), 1571–
 757 1578, [https://doi.org/10.1175/1520-0485\(1999\)029<1571:TRBEIT>2.0.CO;2](https://doi.org/10.1175/1520-0485(1999)029<1571:TRBEIT>2.0.CO;2).

758 Marshall, J., C. Hill, L. Perelman, and A. Adcroft, 1997: Hydrostatic, quasi-hydrostatic, and
 759 nonhydrostatic ocean modeling. *Journal of Geophysical Research: Oceans*, **102** (C3), 5733–
 760 5752, <https://doi.org/10.1029/96jc02776>.

- Marshall, J., D. Jamous, and J. Nilsson, 2001: Entry, Flux, and Exit of Potential Vorticity in Ocean Circulation. *J. Phys. Oceanogr.*, **31** (3), 777–789, [https://doi.org/10.1175/1520-0485\(2001\)031<0777:EFAEOP>2.0.CO;2](https://doi.org/10.1175/1520-0485(2001)031<0777:EFAEOP>2.0.CO;2).
- Marshall, J., and T. Radko, 2003: Residual-mean solutions for the Antarctic Circumpolar Current and its associated overturning circulation. *Journal of Physical Oceanography*, **33** (11), 2341–2354, [https://doi.org/10.1175/1520-0485\(2003\)033<2341:RSFTAC>2.0.CO;2](https://doi.org/10.1175/1520-0485(2003)033<2341:RSFTAC>2.0.CO;2).
- Marshall, J., and K. Speer, 2012: Closure of the meridional overturning circulation through southern ocean upwelling. *Nature Geoscience*, **5**, 171–180, <https://doi.org/10.1038/ngeo1391>, URL <https://doi.org/10.1038/ngeo1391>.
- Maze, G., J. Deshayes, J. Marshall, A.-M. Tréguier, A. Chronis, and L. Vollmer, 2013: Surface vertical PV fluxes and subtropical mode water formation in an eddy-resolving numerical simulation. *Deep Sea Research Part II: Topical Studies in Oceanography*, **91**, 128–138, <https://doi.org/10.1016/j.dsr2.2013.02.026>.
- Maze, G., G. Forget, M. Buckley, J. Marshall, and I. Cerovecki, 2009: Using transformation and formation maps to study the role of air–sea heat fluxes in North Atlantic Eighteen Degree Water formation. *Journal of Physical Oceanography*, **39** (8), 1818–1835, <https://doi.org/10.1175/2009JPO3985.1>.
- Maze, G., and J. Marshall, 2011: Diagnosing the Observed Seasonal Cycle of Atlantic Subtropical Mode Water Using Potential Vorticity and Its Attendant Theorems. *Journal of Physical Oceanography*, **41**, 1986–1999, <https://doi.org/10.1175/2011JPO4576.1>.
- Olsina, O., N. Wienders, and W. K. Dewar, 2013: An estimate of the climatology and variability of Eighteen Degree Water potential vorticity forcing. *Deep Sea Research Part II: Topical Studies in Oceanography*, **91**, 84–95, <https://doi.org/10.1016/j.dsr2.2013.02.018>.
- Penduff, T., M. Juza, B. Barnier, J. Zika, W. K. Dewar, A.-M. Treguier, and Coauthors, 2011: Sea level expression of intrinsic and forced ocean variabilities at interannual time scales. *Journal of Climate*, **24** (21), 5652–5670, <https://doi.org/10.1175/JCLI-D-11-00077.1>.
- Peng, G., E. P. Chassignet, Y.-O. Kwon, and S. C. Riser, 2006: Investigation of variability of the North Atlantic Subtropical Mode Water using profiling float data and numerical model

output. *Ocean Modelling*, **13** (1), 65–85, <https://doi.org/10.1016/j.ocemod.2005.07.001>, URL <https://linkinghub.elsevier.com/retrieve/pii/S146350030500082X>.

Poulsen, M. B., M. Jochum, J. R. Maddison, D. P. Marshall, and R. Nuterman, 2019: A geometric interpretation of southern ocean eddy form stress. *Journal of Physical Oceanography*, **49** (10), 2553–2570, <https://doi.org/10.1175/JPO-D-18-0220.1>.

Rhines, P. B., and W. R. Young, 1982: Homogenization of potential vorticity in planetary gyres. *J. Fluid Mech.*, **122** (-1), 347, <https://doi.org/10.1017/S0022112082002250>.

Ringler, T., J. A. Saenz, P. J. Wolfram, and L. V. Roedel, 2017: A Thickness-Weighted Average Perspective of Force Balance in an Idealized Circumpolar Current. *Journal of Physical Oceanography*, **47** (2), 285–302, <https://doi.org/10.1175/JPO-D-16-0096.1>.

Sinha, A., and R. P. Abernathey, 2016: Time scales of Southern Ocean eddy equilibration. *Journal of Physical Oceanography*, **46** (9), 2785–2805, <https://doi.org/10.1175/JPO-D-16-0041.1>.

Stanley, G. J., T. E. Dowling, M. E. Bradley, and D. P. Marshall, 2020: Ertel Potential Vorticity versus Bernoulli Potential on Approximately Neutral Surfaces in the Antarctic Circumpolar Current. *Journal of Physical Oceanography*, **50** (9), 2621–2648, <https://doi.org/10.1175/JPO-D-19-0140.1>.

Stanley, G. J., and D. P. Marshall, 2022: Why Mean Potential Vorticity Cannot Be Materially Conserved in the Eddying Southern Ocean. *Journal of Physical Oceanography*, **52** (8), 1629–1654, <https://doi.org/10.1175/JPO-D-21-0195.1>.

Stevens, S. W., R. J. Johnson, G. Maze, and N. R. Bates, 2020: A recent decline in North Atlantic subtropical mode water formation. *Nat. Clim. Chang.*, **10** (4), 335–341, <https://doi.org/10.1038/s41558-020-0722-3>.

Treguier, A. M., I. M. Held, and V. D. Larichev, 1997: Parameterization of Quasigeostrophic Eddies in Primitive Equation Ocean Models. *Journal of Physical Oceanography*, **27** (4), 567–580, [https://doi.org/10.1175/1520-0485\(1997\)027<0567:POQEIP>2.0.CO;2](https://doi.org/10.1175/1520-0485(1997)027<0567:POQEIP>2.0.CO;2).

Tsubouchi, T., T. Suga, and K. Hanawa, 2016: Comparison Study of Subtropical Mode Waters in the World Ocean. *Frontiers in Marine Science*, **3**, <https://doi.org/10.3389/fmars.2016.00270>.

- 816 Uchida, T., D. Balwada, Q. Jamet, W. K. Dewar, B. Deremble, T. Penduff, and J. Le Sommer, 2023:
817 Cautionary tales from the mesoscale eddy transport tensor. *Ocean Modelling*, **182**, 102 172,
818 <https://doi.org/10.1016/j.ocemod.2023.102172>.
- 819 Uchida, T., Q. Jamet, W. K. Dewar, J. Le Sommer, T. Penduff, and D. Balwada, 2022: Diagnosing
820 the Thickness-Weighted Averaged Eddy-Mean Flow Interaction From an Eddying North Atlantic
821 Ensemble: The Eliassen-Palm Flux. *Journal of Advances in Modeling Earth Systems*, **14** (5),
822 e2021MS002 866, <https://doi.org/10.1029/2021MS002866>.
- 823 Uchida, T., Q. Jamet, A. C. Poje, N. Wienders, L. Sun, and W. K. Dewar, 2025: Dynamics and
824 thermodynamics of the Boussinesq North Atlantic eddy kinetic energy spectral budget. *Journal*
825 *of Advances in Modeling Earth Systems*, <https://doi.org/10.1029/2024MS004781>.
- 826 Walin, G., 1982: On the relation between sea-surface heat flow and thermal circulation in the
827 ocean. **34** (2), 187, <https://doi.org/10.3402/tellusa.v34i2.10801>, number: 2 Publisher: Stock-
828 holm University Press.
- 829 Warren, B. A., 1972: Insensitivity of subtropical mode water characteristics to meteorological
830 fluctuations. *Deep Sea Research and Oceanographic Abstracts*, **19** (1), 1–19, [https://doi.org/](https://doi.org/10.1016/0011-7471(72)90020-7)
831 [10.1016/0011-7471\(72\)90020-7](https://doi.org/10.1016/0011-7471(72)90020-7).
- 832 Waterman, S., and B. J. Hoskins, 2013: Eddy shape, orientation, propagation, and mean flow
833 feedback in western boundary current jets. *Journal of Physical Oceanography*, **43** (8), 1666–
834 1690, <https://doi.org/10.1175/JPO-D-12-0152.1>.
- 835 Worthington, L. V., 1958: The 18° water in the Sargasso Sea. *Deep Sea Research*, **5** (2), 297–305.
- 836 Young, W. R., 2012: An Exact Thickness-Weighted Average Formulation of the Boussi-
837 nesq Equations. *Journal of Physical Oceanography*, **42** (5), 692–707, [https://doi.org/10.1175/](https://doi.org/10.1175/JPO-D-11-0102.1)
838 [JPO-D-11-0102.1](https://doi.org/10.1175/JPO-D-11-0102.1).